JBC RESEARCH ARTICLE

The calcium-free form of atorvastatin inhibits amyloid-β(1–42) aggregation *in vitro*

Received for publication, December 5, 2021, and in revised form, January 13, 2022 Published, Papers in Press, January 30, 2022,
https://doi.org/10.1016/j.jbc.2022.101662

Hadi Nedaei[1], Nasrollah Rezaei-Ghaleh[2,3], Karin Giller[2], Stefan Becker[2], Leila Karami[4], Ali Akbar Moosavi-Movahedi[1], Christian Griesinger[2,*], and Ali Akbar Saboury[1,*]

From the [1]Department of Biophysics, Institute of Biochemistry and Biophysics (IBB), University of Tehran, Tehran, Iran; [2]Department of NMR-based Structural Biology, Max Planck Institute for Biophysical Chemistry, Göttingen, Germany; [3]Institute of Physical Biology, Heinrich Heine University Düsseldorf, Düsseldorf, Germany; [4]Department of Cell and Molecular Biology, Kharazmi University, Tehran, Iran

Edited by Wolfgang Peti

Alzheimer's disease is characterized by the presence of extraneuronal amyloid plaques composed of amyloid-beta (Aβ) fibrillar aggregates in the brains of patients. In mouse models, it has previously been shown that atorvastatin (Ator), a cholesterol-lowering drug, has some reducing effect on the production of cerebral Aβ. A meta-analysis on humans showed moderate effects in the short term but no improvement in the Alzheimer's Disease Assessment Scale—Cognitive Subscale behavioral test. Here, we explore a potential direct effect of Ator on Aβ42 aggregation. Using NMR-based monomer consumption assays and CD spectroscopy, we observed a promoting effect of Ator in its original form (Ator-calcium) on Aβ42 aggregation, as expected because of the presence of calcium ions. The effect was reversed when applying a $CaCO_3$-based calcium ion scavenging method, which was validated by the aforementioned methods as well as thioflavin-T fluorescence assays and transmission electron microscopy. We found that the aggregation was inhibited significantly when the concentration of calcium-free Ator exceeded that of Aβ by at least a factor of 2. The $^{1}H–^{15}N$ heteronuclear single quantum correlation and saturation-transfer difference NMR data suggest that calcium-free Ator exerts its effect through interaction with the $^{16}KLVF^{19}$ binding site on the Aβ peptide *via* its aromatic rings as well as hydroxyl and methyl groups. On the other hand, molecular dynamics simulations confirmed that the increasing concentration of Ator is necessary for the inhibition of the conformational transition of Aβ from an α-helix-dominant to a β-sheet-dominant structure.

It has been shown that Alzheimer's disease (AD) is characterized by intraneuronal tangles (formed by the accumulation of tau proteins) (1–3) and extraneuronal senile plaques (containing mainly amyloid-beta [Aβ] aggregates) (4, 5) in the brain of patients (6–8). Aβ of different lengths originates from the amyloid precursor protein (APP) embedded in the neural membranes that is cleaved consecutively by β-secretase and γ-secretase. Aβ forms soluble oligomers of different forms or species, which eventually aggregate into much larger insoluble fibrils depositing as plaques. There is so far no consensus on which aggregate species is responsible for neuronal dysfunction and death. However, mounting evidence shows that protein aggregation is of great importance, and blocking it is a valid target for pharmaceutical interventions (9–13).

To prevent Aβ aggregation, several approaches or strategies have been developed in research laboratories around the world (14, 15). These approaches are mainly based on using anti-Aβ antibodies (16–19), small molecules of different classes (20, 21), and peptides of different lengths (22–25). Among these, natural and synthetic small molecules have attracted a lot of attention especially because of their sizes, which enable them to cross the blood–brain barrier more easily, and also their abundance and varieties in the nutritional and botanical resources, which makes them more available. On the other hand, because of obvious differences in the regions of protein–protein and protein–small molecule interaction interfaces, which are approximately 1500 to 3000 $Å^2$ and 300 to 1000 $Å^2$, respectively, many of the small molecules are unable to show a significant effect on the aggregation (26–28). Regarding Aβ, because of being an intrinsically disordered protein (29), the limited structural information on its toxic oligomeric aggregates (30–32), and the polymorphism of its fibrils (33), developing small-molecule inhibitors is further challenging. To find such inhibitors, several small molecules have been examined so far (5, 34). By binding to the N-terminal region of early Aβ oligomers, curcumin and resveratrol inhibit the production of more toxic ones (35). FMeC1 and FMeC2, two derivatives of curcumin with the substitution at the C-4 position, reduce insoluble Aβ deposits as well as cognitive deficits in APPswe–PS1dE9 double transgenic mice more than curcumin itself (36). Resveratrol, on the other hand, can initially accelerate the production of Aβ fibrils by binding to the Aβ hydrophobic domain *via* its phenolic rings. But, by self-stacking of the aromatic residues in the Aβ core domain, these fibrils are then converted to unstructured aggregates. Consequently, the level of aggregation is reduced (37, 38). A key flavonoid of green tea, epigallocatechin-3-gallate (EGCG),

* For correspondence: Ali Akbar Saboury, saboury@ut.ac.ir; Christian Griesinger, cigr@nmr.mpibpc.mpg.de.

causes the formation of nontoxic species by binding to monomeric Aβ (39). Orcein, an organic plant pigment, renders more toxic Aβ oligomeric species into nontoxic fibrillar aggregates (40). Since Aβ fibrils themselves act as secondary nucleation centers of further fibrillation, it has been shown that brazilin, a red dye obtained from *Caesalpinia sappan* heartwood, prevents the act by binding to and remodeling the fibrils. It can also target D23–K28 intermolecular salt bridge formation through hydrophobic interactions with Aβ and thus modulate Aβ aggregation, based on molecular docking studies (41). As a proven inhibitor of the aggregation, Tanshinone I, extracted from *Salvia miltiorrhiza*, prevents the formation of Aβ oligomeric species by binding to I31–M35 and M35–V39 formed C-terminal hydrophobic grooves, based on molecular dynamics (MD) simulations (42).

Much attention has been paid to statins. Statins (β-hydroxy β-methylglutaryl-CoA reductase inhibitors) are a class of cholesterol-lowering drugs commonly employed as a first-line treatment for relieving cardiovascular diseases. The most well-known statins are atorvastatin (Ator; Lipitor), simvastatin (Zocor), lovastatin (Mevacor), rosuvastatin (Crestor), fluvastatin (Lescol), pitavastatin (Livazo), and pravastatin (Pravachol) (43–46). Based on the evidence provided by previous researches, Ator, which is commercialized as Ator-calcium (Ator-Ca; 2:1) trihydrate white crystalline powder (Fig. S1), reduces cerebral Aβ40 and Aβ42 levels and their accumulation in the presenilin–APP mouse model of Alzheimer's amyloidosis (47, 48). It could reduce senile plaques and phosphorylated tau to improve cognitive function in aged APP mice (49). By involving the pathway of reducing farnesyl pyrophosphate in cultured hippocampal neurons, Ator reduced inflammatory responses, improved cognitive deficits and long-term potentiation impairment, and prevented Aβ-induced neurotoxicity (50). In the hippocampus of an Aβ42-induced rat model of AD, it attenuated the production of some cytokines, including interleukin-1β, interleukin-6, and tumor necrosis factor-α (51). By upregulating antioxidant systems in a mouse model of AD, Ator prevented spatial learning and memory deficits (52). As revealed by the presence of 4-hydroxy-2-nonenal and advanced glycation end products in the brains of AD mice, Ator reduced the level of oxidative stress (53).

The effect of Ator on mild to moderate AD was studied in several clinical trials. A recent meta-analysis did not show beneficial effects on the Alzheimer's Disease Assessment Scale—Cognitive Subscale (ADAS-Cog) scale, whereas deceleration in the Neuropsychiatric Inventory (NPI) score rise was observed (54). Developed in the 1980s as a standard of assessing antidementia treatments, ADAS-Cog is often employed in both observational and experimental studies on predementia populations, in which cognitive ability ranges from normal cognition to mild cognitive impairment (55). After a long-term treatment with statins in AD patients, no significant effect on the ADAS-Cog scale was observed (the pooled weighted mean difference = −0.16, with no significant statistical difference [p = 0.206]). However, in AD patients with cholesterol levels ≥200 mg/dl, the change of ADAS-Cog scores in the group treated with Ator for 6 months and the control group was −2.14 ± 1.20 and 0.87 ± 0.77, respectively, with p = 0.045. In another study, after treatment with Ator for 6 months, the change of ADAS-Cog scores in AD patients carrying apolipoprotein E4 gene and control group was −1.77 ± 1.10 and 1.89 ± 0.63, respectively, with p = 0.012. As a result, Ator showed a more beneficial effect in AD patients with high cholesterol levels and apolipoprotein E4 gene carriers (54). Developed by Cummings *et al.* (56) in 1994, NPI is a useful measure for assessing behavior and mood symptoms in dementia patients. The meta-analysis showed that the mean change of NPI scores in the group treated with statins was 1.16 less than that in the control group (the pooled weighted mean difference = −1.16) with a significant statistical difference (p = 0.002). Therefore, statins could improve NPI scores in AD patients (54).

As mentioned previously, Ator contains calcium in its commercialized form. It has been shown previously on Aβ40 that calcium ions promote the oligomerization of the peptide, just similar to the accelerated oligomerization of Aβ40 E22G caused by Glu22Gly mutation, which causes the early onset of AD (57). Since any preparation of Ator will contain calcium ions as an interfering factor, it would be necessary to scavenge the ions prior to study the net effect of Ator on Aβ aggregation.

In Aβ aggregation studies, *in silico* methods such as MD simulations are commonly employed to provide a molecular insight into the remodeling of Aβ monomer and its inhibition by small molecules (58–62). These methods are complementary to the experimental ones such as thioflavin-T (ThT) fluorescence assay, transmission electron microscopy (TEM), CD spectroscopy, and NMR-based monomer consumption assay (MCA).

In this project, using spectroscopic, microscopic, and computational techniques, we set out to clarify whether there is a direct effect of Ator on Aβ42 aggregation that might be related to the clinical observations. First, the aggregation in the presence and absence of Ator-Ca and $CaCl_2$ was examined. Afterward, by establishing a specific protocol for scavenging calcium ions, the effect of calcium-free atorvastatin (Ca-free Ator) on the aggregation was studied. Finally, using advanced NMR techniques and a systematic computational study, the mechanism of interaction between Aβ42 and Ca-free Ator was revealed. Our results showed that Ca-free Ator, not Ator-Ca, has the potential to ameliorate Aβ42 aggregation.

Results

Measurement of calcium content of Ator-Ca stock

Using Patton–Reeder Ca^{2+} indicator and UV–visible spectroscopy

To measure the calcium content of Ator-Ca (which contains 2 Ator + 1 Ca) stock using the Ca^{2+} ion indicator Patton–Reeder (PR), first of all, it is necessary to work in a concentration range of the indicator in which it shows a linear response. Therefore, a dilution series of the indicator was prepared at pH 12 and assayed using UV–visible spectroscopy at 400 to 700 nm. As shown in Fig. S2*A1*, PR showed an absorption with a maximum at 637 nm, which drops as the

concentration is reduced. Drawing PR absorbance at 637 nm against its concentration led to a power curve (Fig. S2*A2*), which shows linearity around 0.02 mg/ml.

At this specific concentration of PR, a dilution series of $CaCl_2$, as a reference compound of calcium ions, was prepared and assayed using UV–visible spectroscopy (Fig. S2*B1*) for drawing a calibration curve. The addition of calcium ions, and consequently the formation of PR-Ca complexes, caused a reduction in PR absorption together with a blue shift of its maximum from 637 to 565 nm. The calibration curve was drawn by calculating and normalizing areas under curves of *A* between 420 and 720 nm as a function of $CaCl_2$ concentration (Fig. S2*B2*). Matching Ator-Ca working concentrations (50, 125, and 250 μM) with the curve showed that the Ca ion content of Ator-Ca preparation is close to the stoichiometric Ator:Ca ratio of 2:1.

Using EDTA and NMR spectroscopy

To further verify the stoichiometric ratio of Ator:Ca (2:1), 1D ^{1}H NMR spectra of free EDTA, EDTA–Ca, and EDTA–Ca* were recorded, overlaid, and their intensities compared with each other (Fig. S3). Those peaks belonging to free EDTA appeared at 2.99 and 3.44 ppm. The minor peak at 2.57 ppm is most probably from minor amounts of calcium ions that are already in the EDTA sample and bound to EDTA. The addition of half-stoichiometric amounts of $CaCl_2$ caused a significant intensity gain of the peak at 2.57 ppm and the quartet at 3.13 ppm stemming from the methylene groups of the acetic acids of EDTA. The peaks of free EDTA at 2.99 and 3.44 ppm shifted to 3.05 and 3.49 ppm, respectively, together with a reduction of intensity by a factor of 2. The addition of Ator-Ca dissolved in methanol resulted in a very similar spectrum, with only slightly different chemical shifts of the free EDTA resonances at 2.99 and 3.44 ppm to 3.03 and 3.48 ppm, respectively. Thus, the same amount of EDTA–Ca complex was formed, and the same amount of free EDTA remained in both EDTA–Ca and EDTA–Ca* samples. In other words, the concentration of calcium ions in 250 μM $CaCl_2$ and 250 μM Ator-Ca is the same.

Scavenging calcium ions from Ator-Ca stock

Next, we developed a protocol to scavenge calcium ions of the Ator-Ca stock based on the formation and precipitation of $CaCO_3$ in methanol. First, the absorption of a PR solution was assayed using UV–visible spectroscopy (Fig. S4*A*). The addition of an aliquot of 4.0 mM Ator-Ca to the PR solution caused a reduction in the PR absorption together with its maximum blue shift. Mixing an aliquot of 4.0 mM Ator-Ca and 4.0 mM $NaHCO_3$ with the PR solution caused also a decrease in the PR absorption, but this time without the blue shift, which indicates that a lower amount of calcium ions remained in the mixture, that is, the higher the concentration of $NaHCO_3$, the lower the amount of remaining calcium ions after centrifugation. When $NaHCO_3$ concentration reached 10 mM, nearly all the calcium ions were scavenged from the Ator-Ca stock so that its absorption was almost the same as the PR absorption. The results showed that scavenging all calcium ions of 4.0 mM Ator-Ca in methanol required at least 10 mM $NaHCO_3$. On the other hand, to check Ator concentration in the mixtures, its absorption at 200 to 320 nm was assayed. As shown in *B* of Fig. S4, Ator concentration remained unchanged even after centrifugation.

1D ^{1}H NMR spectra of Aβ42

Gradual conversion of monomeric Aβ to the large oligomers and fibrils during aggregation leads to a decrease of the strong signals of the monomer because of its consumption, as the peaks of oligomers and aggregates cannot be detected by solution-state NMR. Accordingly, real-time NMR experiments are frequently utilized to monitor the time-dependent monomer consumption of Aβ and other proteins during aggregation. To choose an appropriate Aβ42's NMR signal for such an MCA, the 1D ^{1}H NMR spectra of 25 μM Aβ42 before and after incubation for 5 and 10 h were recorded on a 600 MHz NMR spectrometer (Fig. S5). Overlaying the spectra showed that the NMR signals of Aβ42 were almost uniformly decreased in methyl, aliphatic, aromatic, and amide regions. The signals at 0.65 to 1.0 ppm, which belong to the side-chain methyl groups of residues, Val, Leu, and Ile, had higher intensities compared with the other regions and were therefore chosen as the most sensitive probes for the MCA of Aβ42 in the presence and absence of Ator. Thus, these signals are far from the buffer and Ator signals, further simplifying their use in MCAs.

Effect of Ator-Ca and $CaCl_2$ on Aβ42 aggregation

MCA was employed to study the effect of Ator in its original formulation (Ator-Ca) on Aβ42 aggregation. The calculation of normalized integration of Aβ42's methyl signal declined for 10 h, and drawing its value against the time of incubation (in hours) delivered a reverse sigmoidal curve containing initial, middle, and final stages of the consumption with different slopes (Fig. 1). The same procedure was applied for Aβ42 treated separately with 125 and 250 μM Ator-Ca and $CaCl_2$. As shown in Figure 1*A1*, treatment with Ator-Ca accelerated the monomer consumption by shortening the initial stage without a significant effect on the middle stage. The presence of calcium ions in Ator-Ca prompted us to apply MCA for Aβ42 treated with $CaCl_2$ as a net Ca ion resource (Fig. 1*A2*). The experiment showed that calcium ions promote Aβ42 aggregation by shortening the initial stage as well. Therefore, to observe a net effect of Ator on the aggregation, we needed to use our Ca-free Ator preparation.

Effect of Ca-free Ator on Aβ42 aggregation

After scavenging calcium ions of Ator-Ca stock, multiple techniques such as MCA, CD spectroscopy, ThT fluorescence assay, and TEM were employed to study the effect of the Ca-free Ator on Aβ42 aggregation, as follows:

Aβ42 MCA when treated with Ca-free Ator

MCA was measured for samples containing 25 μM Aβ42 treated with 0, 50, 125, and 250 μM Ca-free Ator (Fig. 1*B*).

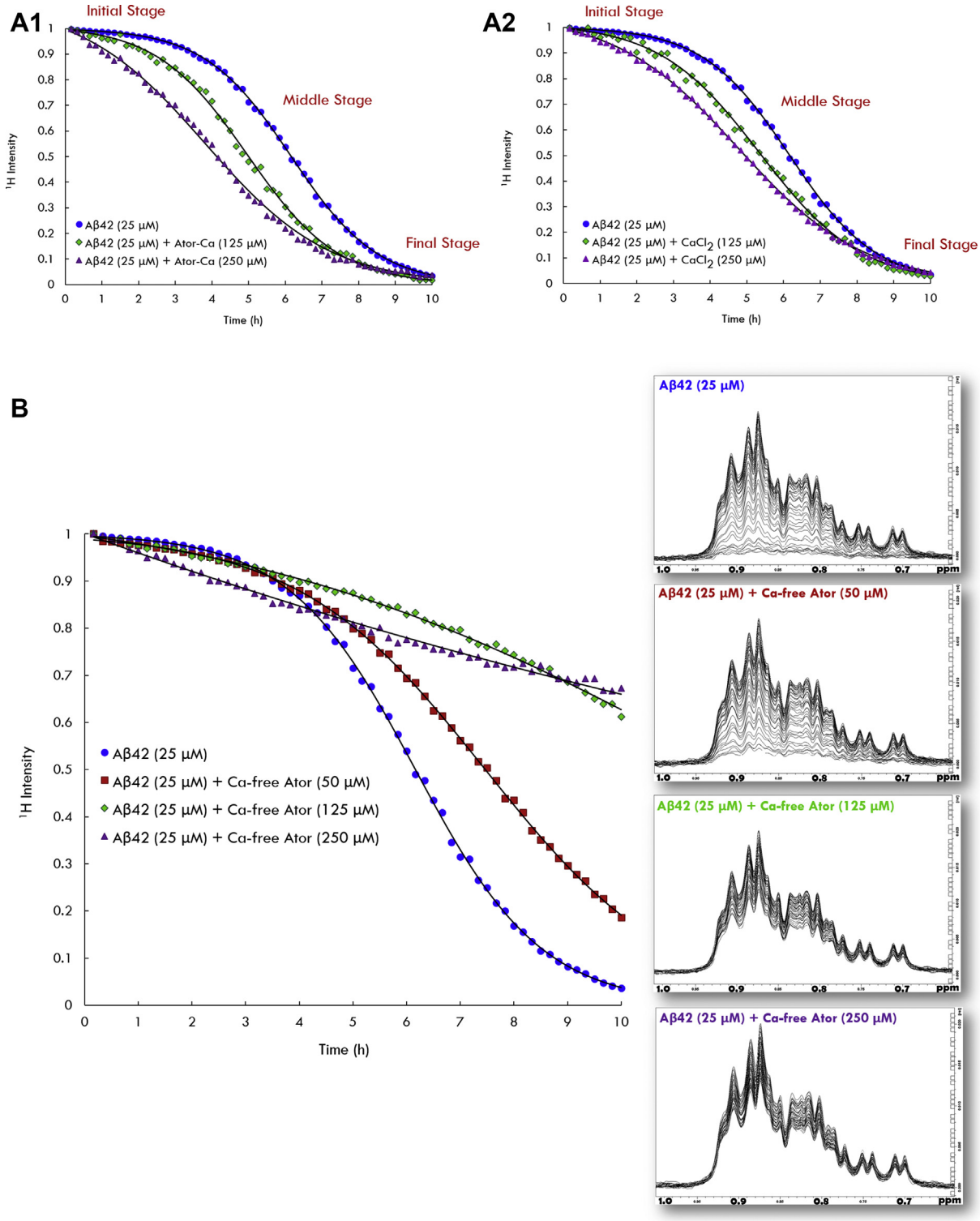

Figure 1. Effect of the increasing concentration of calcium-containing atorvastatin (Ator-Ca) and $CaCl_2$ on Aβ42 aggregation, as revealed by NMR-based MCA. About 25 μM Aβ42 shows a reverse sigmoidal monomer consumption with a linear phase during 2 to 3 h and then the acceleration of the monomer consumption. Monomers are almost completely consumed after an incubation for 10 h. Compared with the control sample, treatment of Aβ42 with 125 μM Ator-Ca (or $CaCl_2$) and 250 μM Ator-Ca (or $CaCl_2$) results in a dose-dependent acceleration of the aggregation by shortening the initial stage, which indicates the promoting effect of calcium ions on the Aβ42 aggregation. *B*, MCA of Aβ42 treated with Ca-free Ator. *Left side*, treatment with 50, 125, and 250 μM Ca-free Ator does not influence the initial rate of consumption, but less acceleration is observed, and considerable amounts of monomer are left after 10 h in a dose-dependent fashion. The sample containing 250 μM Ca-free Ator shows a deviating behavior, that is, the initial rate of monomer consumption is three times that of all the other samples, but no acceleration of monomer consumption is noted during the 10 h observation time. *Right side*, representation of CH_3 NMR signal decay. As shown, the NMR signal of the control sample decays completely into the noise. After 10 h, with 50 (125, 250) μM Ca-free Ator, approximately 20% (65%, 70%) of the monomer NMR signal remains. Ca-free Ator, calcium-free atorvastatin; MCA, monomer consumption assay.

MCA of Aβ42 alone delivered a reverse sigmoidal curve with around 3 h initial stage and reached a plateau after 10 h of incubation at 37 °C. As shown by declining ^{1}H signal intensities at 0.65 to 1.0 ppm, the more the Aβ42 monomers are included in the structure of large NMR-invisible amyloid species, the closer the Aβ42's NMR signal gets to the noise. Treatment with 50 μM Ca-free Ator showed a delay in the middle stage so that NMR signal decay did not reach a plateau after 10 h. Its corresponding declining ^{1}H signal intensities showed some NMR signals left above the noise level. About 125 μM Ca-free Ator caused a much slower decay of Aβ42's NMR signal so that the last NMR spectrum recorded had still a much higher signal above the noise. Treatment with 250 μM Ca-free Ator, on the other hand, caused a completely different monomer consumption. As shown in Figure 1, its MCA was almost linear in shape with no initial stage. However, the slope of the decay was gentle, and the final NMR signal remained largely far from the noise after 10 h.

CD spectroscopy

To investigate Aβ42's secondary structure in the presence and absence of Ator-Ca, $CaCl_2$, and Ca-free Ator, CD spectroscopy was employed. Before incubation in the aggregation-promoting condition (37 °C), Aβ42 showed a far-UV CD spectrum typical of disordered proteins with a deep negative peak around 200 nm. After incubation at 37 °C for 10 h, the CD spectrum of Aβ42 was transformed into the characteristic spectra of β-sheet–rich fibrils with a negative peak around 218 nm. In the presence of Ator-Ca and $CaCl_2$, the negative peak became more intense, suggesting the formation of more β-sheet (Fig. 2*A*). This observation is in line with the MCA data and potentially because of the promoting effect of calcium. On the other hand, when calcium ions of Ator-Ca were scavenged, a concentration-dependent inhibitory effect of Ator on Aβ42 aggregation was observed (Fig. 2*B*).

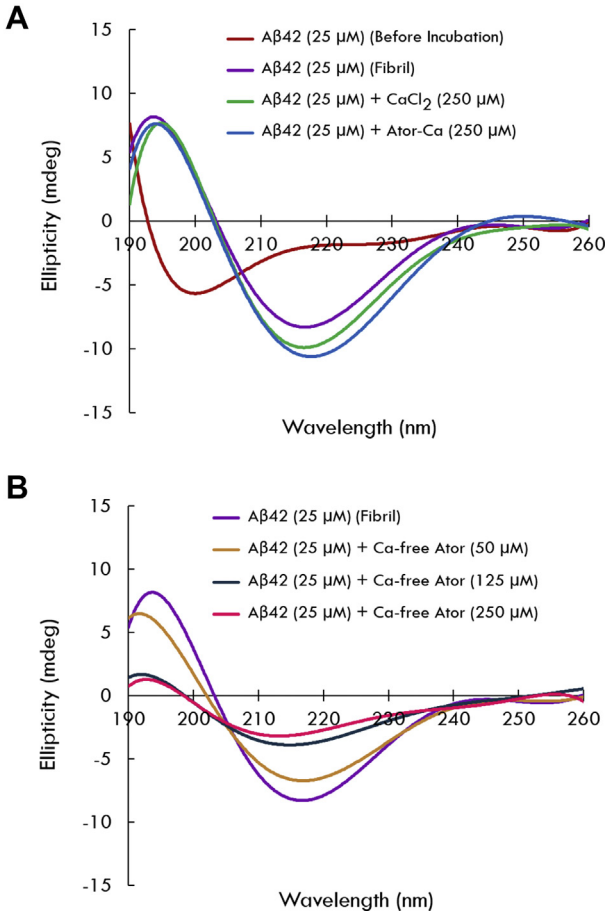

Figure 2. Analysis of Aβ42 secondary structures in the presence and absence of Ator-Ca, $CaCl_2$, and Ca-free Ator. As shown in *A*, monomeric Aβ42's spectrum shows a valley around 200 nm, which is shifted to 218 nm as Aβ42 is aggregated into β-sheet–rich fibrils. Treatment of Aβ42 with Ator-Ca and $CaCl_2$ resulted in deepening the valley, suggesting the aggregation-promoting effect of calcium ions. *B* shows the inhibitory effect of Ca-free Ator on Aβ42 aggregation so that the higher the concentration, the stronger the effect. Ator-Ca, atorvastatin-calcium; Ca-free Ator, calcium-free atorvastatin.

ThT assay

ThT assay data for 25 μM Aβ42 samples containing 0, 50, 125, and 250 μM Ca-free Ator are shown in Figure 3. The ThT intensity of the control sample (without Ator) had grown after 1 h of incubation. Aggregation slowed down after 10 h. When Aβ42 was treated with 50 μM Ca-free Ator, ThT intensity growth experienced a deceleration in the middle stage, and the 10 h intensity value was lower than that of 25 μM Aβ42 in the absence of Ator. At Ca-free Ator concentration of 125 μM (250 μM), a significant reduction in ThT intensity at 10 h was observed to about 40% (20%) of that of the control sample.

TEM

After 10 h of incubation, TEM was employed to examine the morphology of Aβ42 amyloid species produced in the presence of 0 and 250 μM Ca-free Ator (Fig. 4). Incubation of Aβ42 alone caused the production of fibril clumps (Fig. 4, *A*1 and *A*2). A close-up view revealed that they are unbranched micrometers-long twisted fibrils (Fig. 4, *A*3 and *A*4). TEM of the sample containing 250 μM Ca-free Ator showed no fibril clump, but only a few sparse fibrils could be found on the grid (Fig. 4, *B*1–*B*4). These morphological studies have shown that Ator lowers the number of fibrils and accordingly prevents their clumping together.

^{1}H–^{15}N heteronuclear single quantum coherence

To probe the interaction between Ca-free Ator and monomeric Aβ42 at the single-residue resolution, the ^{1}H–^{15}N heteronuclear single quantum coherence (HSQC) spectra of Aβ42 were measured in 0 and 500 μM Ca-free Ator at 278 K (Fig. 5*A*). These conditions (5 °C) deviate from the conditions for aggregation (37 °C). The residue-specific intensity and chemical shift perturbations of Aβ42 were then analyzed (Fig. 5, *B* and *C*). In the presence of Ca-free Ator, Aβ42's amino acids showed a nearly uniform intensity gain over the peptide sequence (Fig. 5*B*). The gain in the intensity could have its root in several mechanisms, for example, the addition of Ator might have reduced the base-catalyzed water–amide proton exchange rates or diminished Aβ's dynamics at

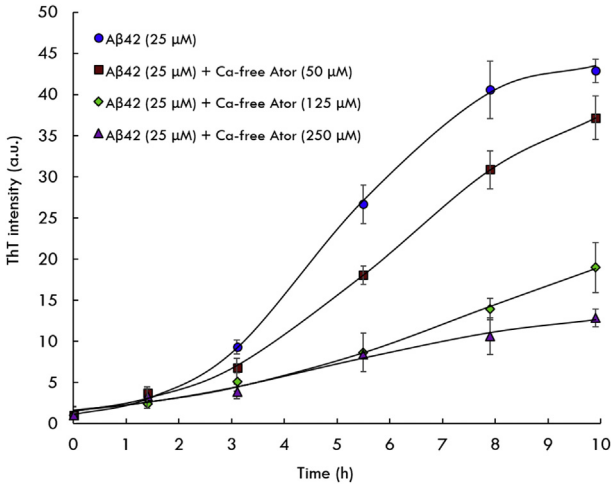

Figure 3. ThT assay of Aβ42 aggregation in the presence of Ca-free Ator. Drawing ThT intensity value against the time of 25 μM Aβ42 incubation in the presence of 0, 50, 125, and 250 μM Ca-free Ator at 37 °C showed that as the concentration of Ca-free Ator increased, the rise of ThT intensity decreased. The ameliorating effect of Ca-free Ator was such that with 125 μM of it, ThT intensity reached about 0.4 of that of the control sample (without Ator) and about 0.2 when treatment with 250 μM Ca-free Ator is done. Error bars are standard deviations obtained from triplicate samples. Thus, the differences are significant. Ca-free Ator, calcium-free atorvastatin; ThT, thioflavin-T.

micro-to-millisecond timescales. Alternatively, it could be caused by Ator-induced disassembly of preformed Aβ42 aggregates. Chemical shift analysis (Fig. 5*C*) showed that the largest perturbation occurred at K16, L17, V18, and F19. Overall, our data suggest a transient weak interaction between Ator and Aβ42 and refer to the stretch of hydrophobic residues L17–V18–F19 as a potential interaction site for the large aromatic system of Ator.

Saturation-transfer difference NMR

To further investigate the weak interaction of Aβ42 with Ca-free Ator, the saturation-transfer difference (STD)-NMR method was employed (Fig. 6). STD-NMR is a powerful tool in detecting weak interactions between small-molecule ligands and macromolecular proteins and is widely used in ligand screening against pharmacological protein targets (63). In the STD approach, a proton signal from the protein of interest is irradiated and saturated for a sufficiently long time, during which the saturation will be transferred through dipolar crossrelaxation to all the other protons of the protein as well as those of the ligand, which come into close contact with the protein protons during the saturation period. The saturation transfer–induced reduction in the intensity of ligand signals will then identify a binding event. As shown in Figure 6*A*, a saturation of Aβ42 at 0.85 ppm, a frequency belonging exclusively to the side-chain methyl groups of Aβ42, resulted in the STD of Ator's signals, mainly of its methyl and aromatic groups. When the saturation frequency was shifted upfield to 0.0, −0.5, and −1.0 ppm where the largely broadened invisible signals of Aβ aggregates exist, the STD intensities of methyl and aromatic groups of Ator were still detectable, albeit at lower intensities. The STD-NMR data, therefore, support the presence of weak transient interaction between Ator and Aβ42 in monomeric and aggregated states. Further experiments are however needed to determine the relative contribution of Aβ42 monomers and oligomeric aggregates in transient interactions with Ator.

MD simulations

After doing three 500-ns MD simulations of different molar ratios (Aβ42:Ator [1:2], Aβ42:Ator [1:5], and Aβ42:Ator [1:10]), the analysis of MD trajectories was performed using the analysis tools of GROMACS (gmx rms for RMSD, gmx rmsf for root mean square fluctuation [RMSF], gmx gyrate for radius of gyration [Rg], gmx hbond for number of hydrogen bonds [h-bonds], gmx do_dssp for the secondary structure of protein, gmx mindist for number of contacts, and gmx analyze for probability distribution).

To investigate the Aβ42 structural stability and compare it in three simulations, RMSDs of the Aβ42's Cα atoms relative to the starting structures were calculated and shown in Fig. S6*A*. The time evolution plot of RMSD shows that in Aβ42:Ator (1:10) system, the RMSD value converged after 38 ns of the simulation. For other systems, Aβ42 achieves equilibrium in about 200 ns and remains stable until the end of the simulation. The mean values of RMSD for the Aβ42:Ator (1:2), Aβ42:Ator (1:5), and Aβ42:Ator (1:10) systems are 0.96, 0.85, and 0.81 nm, respectively. Since the lowest RMSD value belongs to the Aβ42:Ator (1:10) system and also it has less fluctuation in RMSD value, it can be concluded that there are significant changes in the conformation of Aβ42 peptide in Aβ42:Ator (1:2) and Aβ42:Ator (1:5) systems. This result is consistent with the defined secondary structure protein (DSSP) analysis.

For a better evaluation, the probability distribution of each RMSD value was calculated and depicted in Fig. S6*B*. Aβ42:Ator (1:10) shows a high and narrow RMSD probability distribution peak around 0.81 nm, which corresponds to the average value of the RMSD, compared with other systems. This indicates the more stable conformational dynamics of Aβ42:Ator (1:10) than other systems. Aβ42:Ator (1:2) and Aβ42:Ator (1:5) systems display similar RMSD distributions, three wide peaks near 0.6 to 1.3 nm. The height of some peaks in Aβ42:Ator (1:5) is more than Aβ42:Ator (1:2).

Fig. S6*C* shows the RMSFs of Cα atoms in Aβ42 in all simulated systems. C-terminal residues (38–42) of Aβ42:Ator (1:2) and N-terminal residues (1–5) of all systems show the greatest fluctuations. This panel clearly shows small RMSF values or small conformational fluctuations in Aβ42:Ator (1:10) compared with the Aβ42:Ator (1:2) and Aβ42:Ator (1:5), indicating that Aβ42 is more involved in interaction with Ator molecules in this system. This can be attributed to the higher number of Ator molecules. It can also be seen that residues 15 to 21 have the lowest fluctuation in Aβ42:Ator (1:10) system.

To estimate a general dynamic behavior of the Aβ42 structure, the Rgs were calculated during the MD simulations (Fig. S6*D*). As can be seen from this figure, Aβ42:Ator (1:5) has

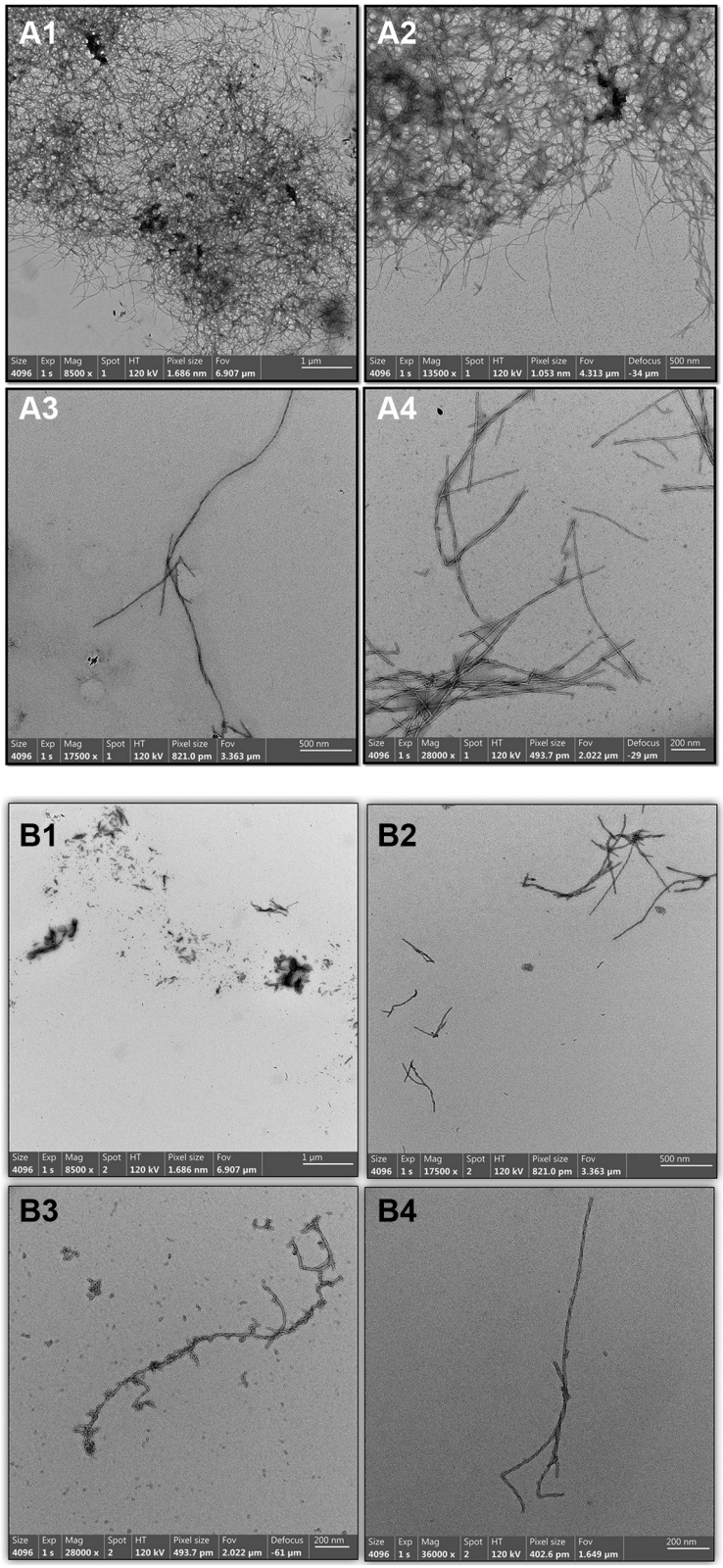

Figure 4. TEM of Aβ42 amyloid species produced in the presence of 0 and 250 μM Ca-free Ator after an incubation for 10 h. As shown in the *A1–A4* with different magnification, 25 μM Aβ42 incubation produced a large amount of micrometers-long unbranched fibrils, many gathered together as clumps (*A1* and *A2*). In the presence of 250 μM Ca-free Ator (*B1–B4*), no fibril clump was observed, and only few sparse fibrils could be found on the grid. Ca-free Ator, calcium-free atorvastatin; TEM, transmission electron microscopy.

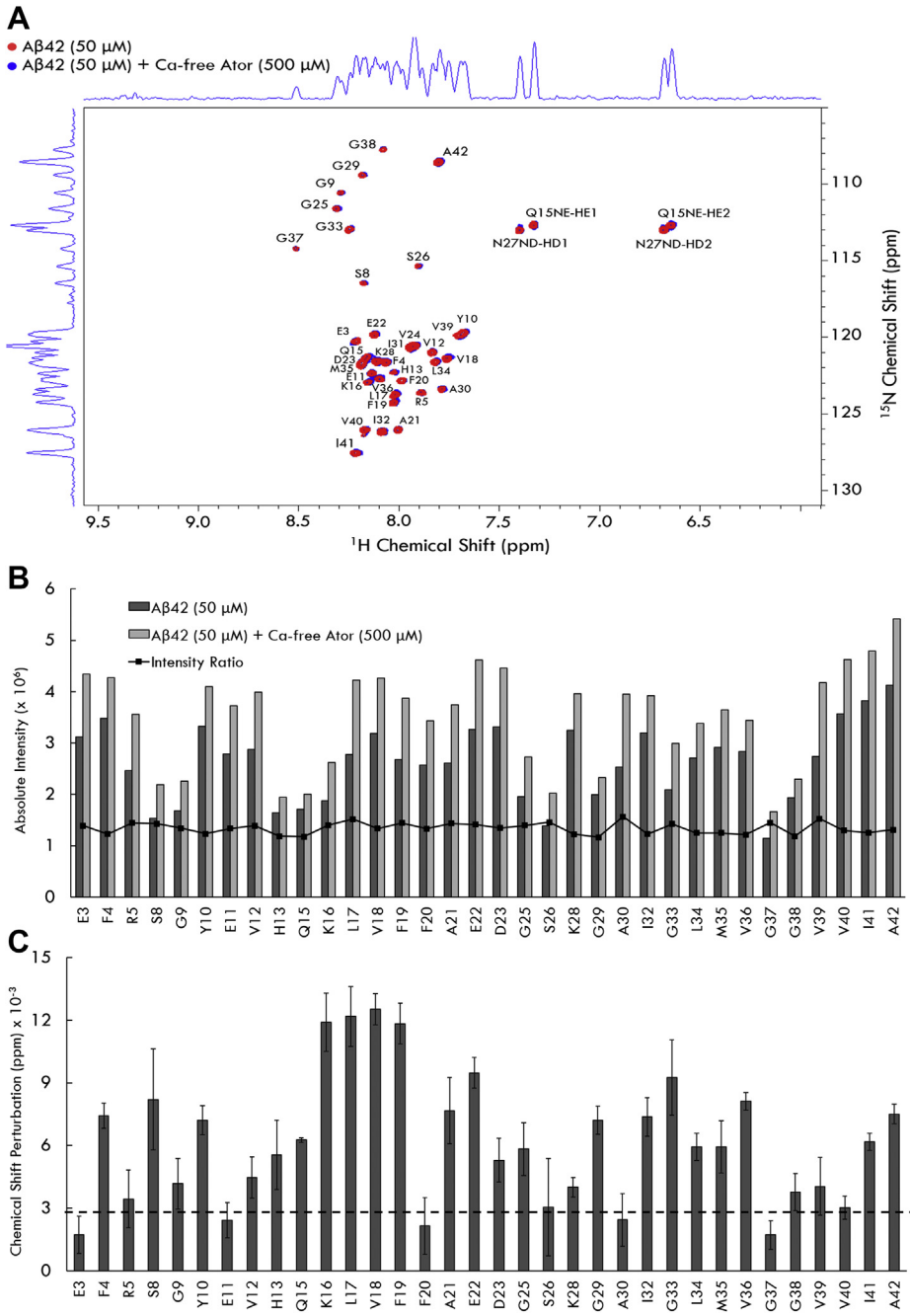

Figure 5. Interaction of monomeric Aβ42 with atorvastatin (Ator) probed at single-residue resolution. *A*, shows the ^{1}H–^{15}N HSQC spectra of 50 μM monomeric Aβ42 treated with 0 (*red*) or 500 μM Ca-free Ator (*blue*). *B*, shows Ator-induced perturbations in the intensity of Aβ42's crosspeaks over the peptide sequence. A nearly uniform intensity gain is observed along the Aβ42 sequence. *C*, shows the combined ^{1}H,^{15}N chemical shift perturbation of Aβ42 induced by Ator as a function of residue number. Residues K16, L17, V18, and F19 exhibit the largest chemical shift perturbations, when compared with the background chemical shift variation (presented as the *dashed line*). Ca-free Ator, calcium-free atorvastatin; HSQC, heteronuclear single quantum coherence.

the most fluctuation and greater value of Rg relative to other systems, indicating the maximum variations in the structural compactness of Aβ42. This can be attributed to the second structure of the peptide. The average number of residues adopting β-sheet and α-helix in Aβ42:Ator (1:2) and Aβ42:Ator (1:10) systems, respectively, is more than that of Aβ42:Ator (1:5) (Figs. 7*A* and 8*A*).

Secondary structure analysis was done using the DSSP program (64). The time evolution of the secondary structures of Aβ42 at different Aβ42–Ator molar ratios is illustrated in Figure 7. Figure 7*A* shows the initial structure of Aβ (Protein Data Bank [PDB] ID: 2LFM). In Aβ42:Ator (1:2) system (Fig. 7*B*), residues 28 to 38 form β-sheet structures linked with turn after 95 ns. Indeed, this concentration of Ator cannot prevent the conformational transition from random coil/α-helix to β-sheet well. Residues 13 to 24 keep their α-helix and 3_{10}-helix structures, except 350 to 450 ns. Also, residues 5 to 13 have greatly turn structure from 45 ns to the end of

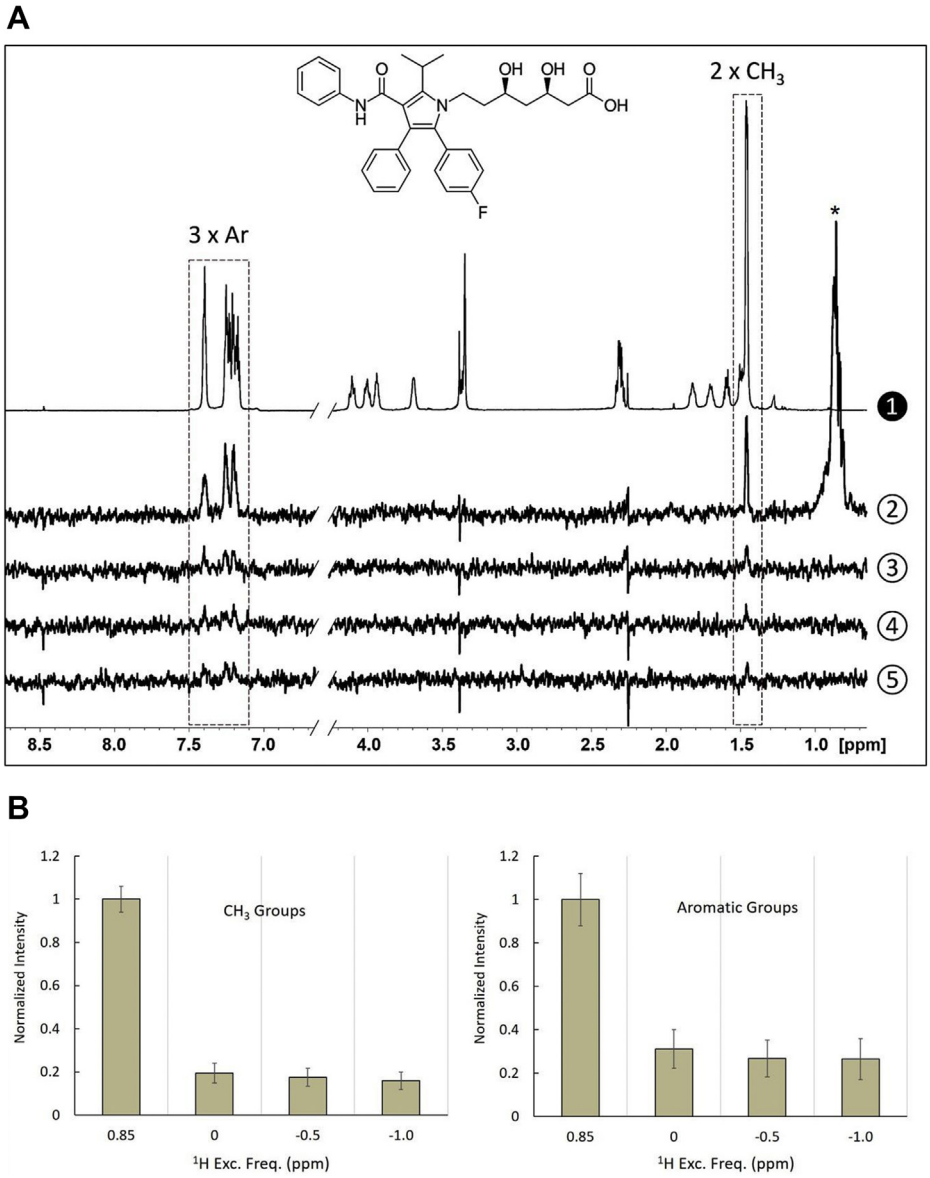

Figure 6. STD-NMR of 5.0 μM Aβ42 in the presence of 300 μM Ca-free Ator at 310 K. *A*, Ator's 1D ^{1}H NMR spectrum was used as a reference (❶). The saturation of Aβ42 at 0.85 ppm resulted in the appearance of Ator's STD signals belonging to its CH_3 and aromatic groups (②). The NMR signal marked by *asterisk* belongs to Aβ42's CH_3 groups saturated at this frequency. Aβ42 saturation at 0 (③), −0.5 (④), and −1.0 (⑤) ppm, resulted in a similar phenomenon so that the saturation was transferred to Ator's CH_3 and aromatic groups. *B*, normalized intensity of Ator's signals as a function of Aβ42 ^{1}H saturation frequency showed that there is a significant interaction between Ator and Aβ42 oligomers. Ca-free Ator, calcium-free atorvastatin; STD, saturation-transfer difference.

simulation time. In Aβ42:Ator (1:5) system (Fig. 7*C*), the β-sheet formation has been significantly reduced compared with the Aβ42:Ator (1:2) system, so that there is no β-sheet structure at the end of the simulation time. As can be seen, most residues switch dynamically between the bend and turn conformations during the simulation time. Some residues show α-helix and 3_{10}-helix conformations. In Aβ42:Ator (1:10) system (Fig. 7*D*), no β-sheet conformation is seen throughout the simulation time. Compared with Aβ42:Ator (1:2) and Aβ42:Ator (1:5) systems, the turn has been reduced. Residues K16, L17, V18, and F19 contribute to α-helix and 3_{10}-helix conformation in the high fraction of simulation time. From DSSP analysis, it can be concluded that the prevention of the conformational transition of Aβ42 depends on the Ator concentration.

Also, the average number of residues adopting α-helix, 3_{10}-helix, β-sheet, β-bridge, turn, bend, and coil secondary structural elements was calculated for each of the simulated. Figure 8*A* shows the change in secondary structural elements in detail and quantitatively. As the Ator concentration increases, the β-sheet (4:3:0) and turn (14:6:4) content decreases, and α-helix (1:2:4) and coil (13:16:20) content increases.

To investigate the molecular interactions, the time evolution of h-bond formation between Aβ42 and Ator molecules was calculated and plotted in Figure 8*B*. We also obtained the occupancy (percentage) of h-bonds (Table S2). The distance

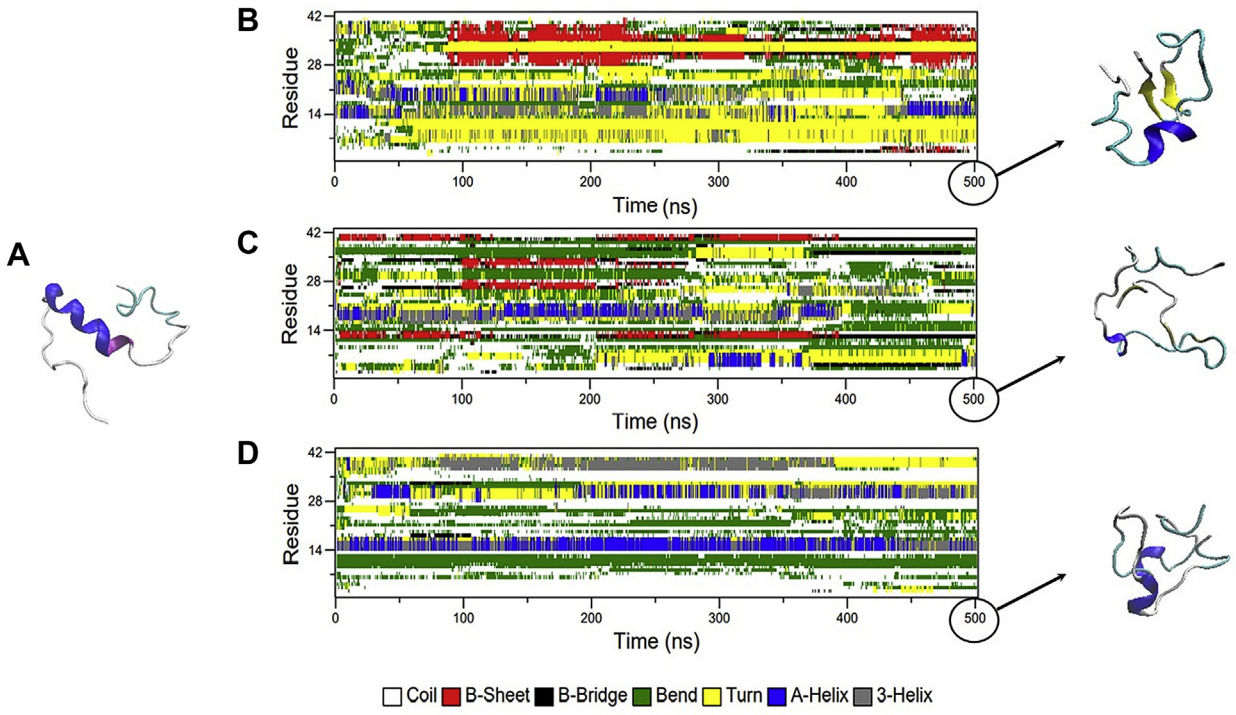

Figure 7. Secondary structure analysis of various Aβ42-Ator systems using the DSSP program. *A*, initial structure of Aβ (Protein Data Bank ID: 2LFM). Time evolution of the secondary structures of Aβ42 for Aβ42:Ator (1:2) (*B*), Aβ42:Ator (1:5) (*C*), and Aβ42:Ator (1:10) (*D*) systems. As shown, as the concentration of Ator increases, the conformational transition of residues 28-38 to β-sheet structures is prevented. Ator, atorvastatin.

cutoff of 3.5 Å between the donor and acceptor atoms and an angle cutoff of 30° were considered for geometry criteria for h-bond analysis. As shown in Figure 8*B*, as the concentration of the Ator molecules increases, the number of intermolecular (Aβ42–Ator) h-bonds increases. More details about these h-bonds are collected in Table S2. In Aβ42:Ator (1:2) system, the carboxyl oxygen atoms of Ator molecules take part in h-bonds with Arg 5. In Aβ42:Ator (1:5) system, in addition to carboxyl oxygen atoms (hydrogen bonded to Lys 16), hydroxyl groups of Ator molecules form h-bonds with Aβ42 peptide (hydrogen bonded to Val 39 and Ala 42 residues). Moreover, h-bonds were also observed between the carbonyl oxygen atoms of Ator molecules and Aβ42 peptide residues, in Aβ42:Ator (1:10) system. With a glance at Table S1, it can be understood that both the number of h-bonds and occupancy (percentage) in the Aβ42:Ator (1:10) system is greater than that of Aβ42:Ator (1:5) and Aβ42:Ator (1:2) systems, respectively.

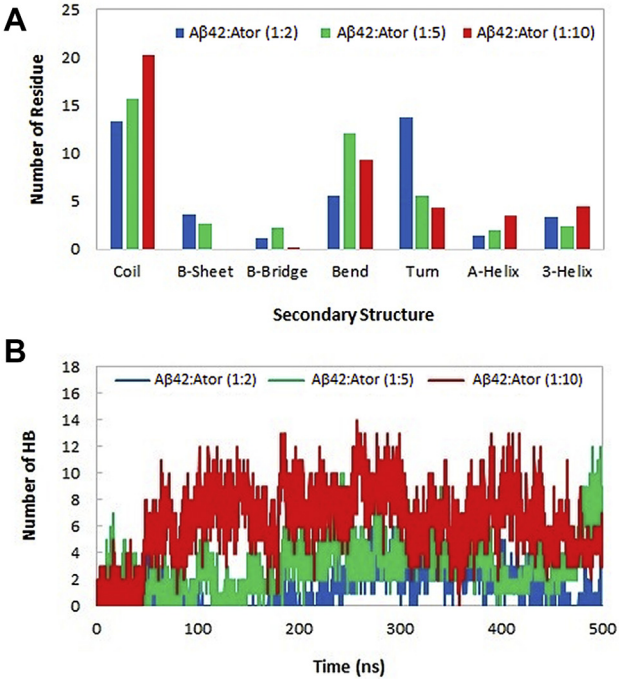

Figure 8. A number of Aβ42's residues adopting secondary structural elements as well as the number of HBs formed in the various Aβ42-Ator systems during the MD simulations. *A*, analysis of secondary structure. Number of residues adopting secondary structural elements was determined. *B*, number of HBs during the MD simulations for Aβ42:Ator (1:2), Aβ42:Ator (1:5), and Aβ42:Ator (1:10) systems. Ator, atorvastatin; HB, hydrogen bond; MD, molecular dynamics.

The number of nonpolar contacts between Ator molecules and the Aβ42 residues was calculated (Fig. 9). For this purpose, the cutoff was set as 0.5 nm. As can be seen, as the concentration of the Ator molecules increases, the number of nonpolar contacts between Ator molecules and most of Aβ42 peptide residues, especially in the Aβ42:Ator (1:10) system, increases. Another important point that can be understood from this figure is that in all simulated systems, K16, L17, V18, F19, and A21 residues have the highest number of nonpolar contacts with Ator molecules. This finding is in good consistent with HSQC spectra results (Fig. 5*C*). In Aβ42:Ator (1:10) system, other residues with a high number of nonpolar contacts are E3, G9, E22, D23, and L34.

A snapshot of the interactions between Aβ and Ator molecules in the Aβ42:Ator (1:10) system is illustrated in Fig. S7. Only those residues that have high participation in interaction

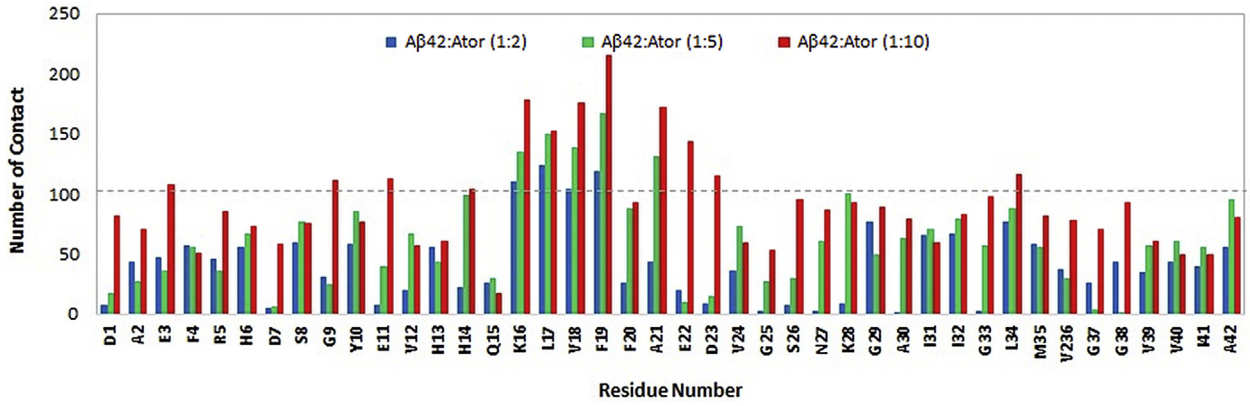

Figure 9. Time-averaged number of nonpolar contacts between Aβ42 residues and atorvastatin (Ator) molecules in Aβ42:Ator (1:2), Aβ42:Ator (1:5), and Aβ42:Ator (1:10) systems. Ator, atorvastatin.

with Ators were considered. The accumulation of Ator molecules around the Aβ42 peptide is well seen in Fig. S7*A*. Fig. S7, *B–E* show the localization and orientation of the Ator molecules in such a way that they have the most interaction with Aβ42 residues. In this regard, we can mention the interactions between the NH_3^+ of Aβ42's K16 and the COO^- of Ator, the isopropyl group of Aβ42's L17/V18 and the same group of Ator, and the phenyl ring of Aβ42's F19 and the same group of Ator.

Discussion

The monomer consumption, ThT fluorescence, CD spectroscopy, and TEM data consistently show that Ator, a commonly used cholesterol-lowering agent, is capable of modulating the *in vitro* aggregation of Aβ42. We provided some experimental evidence that the Ator effect on Aβ42 aggregation varies in dependence on calcium ions: in the presence of calcium ions, it promotes Aβ42 aggregation, whereas in the absence of the ions, an opposite effect is observed. The NMR chemical shift and intensity perturbation analyses and STD-NMR data further support the weak transient interaction between Ator and Aβ42.

Previous *in vitro* and *in vivo* studies have shown that calcium ions are capable of accelerating the aggregation of α-synuclein in free solutions, surfaces, and cytoplasm of cultured cells (65), and the oligomerization of Aβ (57). Since Ator has been formulated as Ator-Ca (2:1) trihydrate, as verified using PR indicator (Fig. S2) and EDTA (Fig. S3), the presence of calcium ions in any Ator preparation will be inevitable; the factor will adversely affect Ator *versus* Aβ aggregation studies, as shown by MCA and CD data (Figs. 1 and 2). To discern a potential inhibitory effect of Ator from the aggregation-promoting effect of Ca^{2+}, we chose to scavenge calcium ions from Ator stock to examine the isolated effect of Ator on Aβ aggregation. Because the concentration of calcium ions inside (∼0.1 μM in the resting state) and outside (1.0–2.0 mM) the mammalian neurons is significantly different, it is expected that the proficiency of Ator would vary between intracellular and extracellular environments such that it could directly prevent the aggregation of intracellular Aβ more effectively than that of extracellular Aβ. Ator has an indirect antiaggregation potential so that it reduces brain Aβ levels by changing the cholesterol metabolism. On average, a 2.5-fold reduction of Aβ40 (from ∼750 to ∼300 pmol/g of the brain hemisphere, with $p < 0.00005$) and an approximately two-fold reduction of Aβ42 (from ∼450 to ∼250 pmol/g, with $p < 0.005$) in the brains of 8-week-old presenilin–APP AD mice treated with Ator (30 mg/kg body weight/day) subsequently led to a ∼2.7-fold decrease (from ∼0.28% to ∼0.08%, with $p = 0.021$) in the Aβ accumulation (47). These results seemed promising but could not be reproduced in humans. Treatment of both 50 normocholesterolemic subjects (<260 mg/dl) (group A) and 50 hypercholesterolemic subjects (≥260 mg/dl) (group B) with the clinically relevant dosage of Ator (10–20 mg) revealed no significant difference in the cerebrospinal fluid Aβ42 concentration between these two groups, tha is, 652.4 ± 192.5 and 698.6 ± 211.3 pg/ml in group A and group B, respectively (66). Therefore, that promising results in mice can be explained by introducing a higher dosage of Ator that can be toxic for humans. Besides, the toxicity of Ator-stabilized Aβ species may vary depending on the presence of calcium ions. Further experiments are required to address these crucial questions.

According to MCA experiments (Fig. 1), Ca-free Ator mainly postpones the initial stage of monomer consumption, which hints at a potential interaction between Ator and early species of Aβ42 amyloidogenesis, mainly monomers and oligomers. However, since the suprastochiometric Ca-free Ator is required to introduce the effect, the interaction is expected to be of weak transient type. To gain further insight into the weak interaction between Ator and the Aβ oligomers, STD-NMR (Fig. 6) was employed. Based on STD-NMR experiments, Ator receives saturation transfer from Aβ42 monomers/oligomers, indicating the presence of weak transient interactions between them. Since this transfer from Aβ42 was mostly to aromatic rings and methyl groups of Ator, a binding epitope on Aβ42 may consist of those residues used to form nonpolar and π–π interactions with ligands. To examine this hypothesis, $^1H–^{15}N$ HSQC was employed (Fig. 5) and

revealed that Aβ42's residues K16, L17, V18, and F19 underwent the largest chemical shift perturbations in the presence of Ator. The sequence ^{16}KLVF^{19} is a major part of a known sequence ^{16}KLVFFA^{21} as an important seeding point in Aβ nucleation-dependent aggregation (67). Therefore, it can constitute a possible binding epitope for Ator in which leucine and valine with isopropyl group side chains and phenylalanine with a benzyl side chain are possibly those sites interacting with methyl and aromatic groups of Ator. Lysine side chain, on the other hand, would be the site to entertain polar contacts with the polar regions of Ator such as hydroxyls and amide group. Previous studies on other inhibitors of Aβ aggregation, such as curcumin, oleuropein, scylloinositol, resveratrol, EGCG, and others, have provided similar results. It has been shown using solid-state NMR that curcumin interacts *via* its methoxy and/or hydroxyl groups with ^{16}KLVFFA^{21} residues of Aβ and *via* its phenolic groups through π-stacking with Tyr, Phe, and His of the peptide (58, 68). Oleuropein (69) and scylloinositol (59) exert their inhibitory effect also by binding to the ^{16}KLVFFA^{21} region. On the other hand, the interaction of resveratrol with residues F4, Y10, F19, and F20 of Aβ (70) shows similarity to some extent with Ator such that chemical shift perturbation of F4 and Y10 was also higher than the threshold (Fig. 5). Another study has shown the strong interaction of EGCG with F19 and 11 more residues of Aβ (39). Molecular docking studies of ^{16}KLVFFA^{21} steric zipper assembly have shown that flavonoid polyphenols, such as myricetin, quercetin, and baicalein, underwent polar contacts by adopting an orientation to the K16 side chain through their 3,4-dihydroxy substituents (71). Based on this observation, the chemical shift perturbation of K16 observed in the presence of Ator could be due to the orientation of Ator's hydroxyl groups to the charged side chain of lysine.

Thus, Ator in the Ca^{2+}-free state is a weak inhibitor of Aβ aggregation using similar binding sites that were described before. Based on the weak interaction and the fact that Ator in the presence of Ca^{2+} ions does not prevent Aβ aggregation, the disease-modifying effects in mice are most probably not because of Aβ aggregation inhibition but to lowering the production of Aβ monomer and consequently its accumulation (47), cutting the tau protein phosphorylation (49), attenuating the production of cytokines (interleukin-1β, interleukin-6, and tumor necrosis factor-α) (51), upregulating antioxidant systems (52), or reducing the level of oxidative stress (as revealed with 4-hydroxy-2-nonenal and advanced glycation end products) (53). Therefore, repurposing this drug for AD could not be hoped for its potential of modulating Aβ aggregation, because with a lot of calcium ions in the extracellular space, the potential would be neutralized. Maybe, the development of Ator analogs could improve its modulating effect on the aggregation. However, in contrast with the extracellular space, the intracellular one contains much fewer calcium ions and is the location of tau aggregation, another signature of AD. Therefore, the investigation of Ator–tau interaction is suggested as a good topic for future studies. Another important point of this study that can be comprehended is the uselessness of an Aβ aggregation modulator in the presence of calcium ions. So, it is strongly encouraged to work in a calcium-containing buffer such as artificial cerebrospinal fluid during the development of Aβ-aggregation–modulating drugs *in vitro*.

Experimental procedures

Materials

Ator-Ca powder was purchased from Morepen Laboratories Ltd. ThT (Chemical Abstracts Service number: 2390-54-7), PR indicator (calconcarboxylic acid; Chemical Abstracts Service Number: 3737-95-9), and other reagents were purchased from Merck KGaA.

Methods

Recombinant production of Aβ42 peptide

A DNA duplex coding for Aβ42 was cloned into a modified pET28a vector. Unlabeled and ^{15}N,^{13}C-labeled Aβ42 fusion protein was expressed in *Escherichia coli* at 37 °C in Toronto minimal medium. After purification on a Protino nickel–nitriloacetic acid column (Macherey–Nagel), the fusion protein was digested overnight at 8 °C with tobacco etch virus protease. The digestion mixture was loaded onto a C4 reversed-phase Vydac HPLC column. The released Aβ42 peptide eluted in a linear (0–100%) acetonitrile gradient from this column as a single peak. The purified peptide was lyophilized before use.

Aβ42 monomerization and aggregation

A monomeric solution of the recombinant Aβ42 was prepared according to the procedure established by Ryan *et al.* (72) with some modifications. In short, Aβ42 powder was dissolved in a 10% ammonia solution (NH_4OH) to prepare a 1.0 mg/ml peptide solution and incubated at room temperature for 10 min, followed by 5 min sonication in a bath sonicator. After lyophilization, the fluffy powder obtained was dissolved in 60 mM NaOH to prepare a 2.0 mg/ml solution and sonicated for one more minute. The solution was then aliquoted in a cold room, flash-frozen in liquid nitrogen, and stored at −80 °C until use. This monomerization procedure, like other ones (https://www.abcam.com/ps/products/120/ab120301/documents/Amyloid%20Beta%20Protocol%20WC050216%20v2%20(website).pdf), cannot provide a completely preaggregate-free Aβ solution. Even if the procedures are very unlikely to be able to provide such a solution, our observations showed that the solution would not be stable even on ice, and there will be some new preaggregates before starting the induction of Aβ aggregation by incubation. Therefore, it is only possible to start with a largely monomeric Aβ solution, not a fully monomerized one.

To induce Aβ42 aggregation, the peptide aliquot was taken out of the −80 °C freezer, quickly thawed, and diluted in a fresh Tris–NaCl buffer (containing 10 mM Tris–HCl, 25 mM NaCl, and 0.02% NaN_3, pH 7.4) to prepare a 25 μM solution. The pH was adjusted to 7.4 using a 100 mM HCl stock and immediately incubated at 37 °C for 10 h.

Preparation of Ator-CA stock

Ator-Ca powder was dissolved in methanol by vortex to prepare a 50 mM stock. The stock was diluted in methanol to make three more stocks with different concentrations (5.0, 10, and 25 mM). All stocks were stored at 4 °C until use.

Measurement of calcium content of Ator-Ca stock

To measure the calcium content of the Ator-Ca stock using PR indicator, a dilution series of it was first prepared in alkaline water (pH 12). Measuring absorption using a UV–visible photometer, a curve of PR's maximum absorbance at 637 nm as a function of its concentration was drawn. This curve was used to find a proper concentration range of the indicator in which its behavior is linear. To obtain a calibration curve of calcium ion content in the presence of the indicator, several samples containing a constant concentration of PR mixed with the increasing concentration of $CaCl_2$ were prepared at pH 12. The absorption of the PR-Ca mixtures was then recorded using the UV–visible photometer. The calibration curve was then drawn as the normalized area under PR-Ca curves at 465 to 720 nm against $CaCl_2$ concentration. As mixed with the same amount of PR, Ator-Ca working concentrations (50, 125, and 250 μM) were assayed using the same UV–visible photometer, and their absorbances were matched on the calibration curve to find their calcium content.

To compare the calcium content of Ator-Ca with that of $CaCl_2$ using EDTA, three samples of free EDTA (0.5 mM), EDTA-Ca (0.5 mM EDTA + 250 μM $CaCl_2$), and EDTA-Ca* (0.5 mM EDTA + 250 μM Ator-Ca), all at pH 12, were prepared and transferred into standard NMR tubes of 3 mm. Then, 1D ^{1}H NMR spectra of the samples were recorded on a 400 MHz Bruker spectrometer at 298 K while using the W5 WATERGATE element for the suppression of the water signal. The spectra were overlaid to compare the absolute intensities of their signals.

Preparation of Ca-free Ator stock

The protocol of Ca-free Ator stock preparation was established based on the formation and precipitation of $CaCO_3$ at pH 12. For this purpose, two separate stocks were prepared, one 25 mM Ator-Ca stock in methanol and the other, 100 mM $NaHCO_3$ stock in alkaline water (pH 12). Aliquots of these two stocks were mixed in methanol such that the final concentrations of Ator-Ca and $NaHCO_3$ were 4.0 and 10 mM (1.0:2.5 ratio), respectively, in the mixture. Following incubation at room temperature for 30 min, solid $CaCO_3$ produced in the mixture was precipitated using centrifugation at 10,000 rpm for 10 min. The supernatant was carefully transferred to another microtube and then acidified to pH 5.0 using HCl. This solution was evaporated using a nitrogen stream, followed by lyophilization. Following the addition of methanol, a concentrated stock of Ca-free Ator was prepared and stored at 4 °C until use. The calcium and Ator contents of the stock were checked with the PR indicator using the UV–visible photometer.

Aβ42 treatment with Ca-free Ator

About 25 μM monomeric Aβ42 solutions were prepared in the Tris–NaCl buffer and mixed with 0, 50, 125, and 250 μM Ca-free Ator on ice. The percentage of methanol in all the samples was set to 1.0%. The pH of the samples was adjusted to 7.4, and then they were immediately incubated at 37 °C for 10 h.

ThT fluorescence assay

To monitor Aβ42 aggregation in the presence of Ca-free Ator using ThT assay, 25 μl of the incubated samples was taken at intervals and mixed with 2.0 ml of a fresh 25 μM ThT stock prepared in the Tris–NaCl buffer. ThT emission was then recorded at 465 to 550 nm using a Varian Cary Eclipse Fluorescence Spectrophotometer with the excitation wavelength of 450 nm. ThT kinetic data were analyzed and fitted to the following logistic equation (73):

$$\ln(F / (F_{\lim} - F)) = kF_{\lim}t + C \quad (1)$$

in which F is time (t)-dependent ThT fluorescence, $F_{\lim}$, its limiting value when $t \to \infty$, k, a tentative rate constant, and C, a constant value.

There is an important point regarding using ThT assay in this study. Since ThT's self-fluorescence is increased at concentrations higher than 5.0 μM (74), it is usually recommended to work with a lower concentration of ThT stock for the assay. However, because of our observation that ThT's interaction with Ator leads to the appearance of white precipitation in the fluorescence cuvette, together with an increase in ThT intensity, we had to work with a higher concentration of ThT, that is, 25 μM, to reduce the effect of the interaction on final intensities as much as possible.

Aβ42 MCA

To monitor the consumption of Aβ42 monomers during the aggregation in the presence and absence of Ca-free Ator, real-time 1D ^{1}H NMR experiments were measured on a 600 MHz Bruker spectrometer equipped with a prodigy cryoprobe. For these measurements, the Aβ samples were prepared at the specified concentrations in the Tris–NaCl buffer, their pH adjusted to 7.4, and transferred into standard NMR tubes of 3 mm. They were then incubated inside a 600 MHz NMR spectrometer at 310 K for 10 h. The temperature calibration was made using a standard thermocouple. The 1D ^{1}H NMR spectra were recorded every 10 min of incubation using the W5 WATERGATE element for the suppression of the water signal. After the spectra collection, the peptide's methyl group signal at 0.65 to 1.0 ppm was monitored, integrated, and normalized, followed by sigmoidal fitting using Equation 1.

CD spectroscopy

Two series of samples were prepared, one containing 25 μM Aβ42 mixed with 250 μM Ator-Ca or $CaCl_2$ in the Tris–NaCl

buffer (pH 7.4), and the other containing the same amount of Aβ42 plus 50, 125, or 250 μM Ca-free Ator prepared in the same buffer. Before and after incubation at 37 °C for 10 h, far-UV CD spectra of the samples were recorded at a JASCO J-815 CD spectropolarimeter. The path length was 1 mm. Each spectrum obtained was then subtracted from the spectrum of the corresponding buffer (containing the same components minus Aβ42), smoothed, and reported as ellipticity (in millidegrees) using the J-810 program.

TEM

For the morphological examination of Aβ42 amyloid species produced in the presence of Ca-free Ator, the 10-h-incubated samples were harvested and poured on carbon-coated copper grids. After staining with 1.0% uranyl acetate, they were analyzed using an FEI CM120 (Talos L120C) transmission electron microscope operating at 120 kV.

^{1}H–^{15}N HSQC spectroscopy

The ^{1}H–^{15}N HSQC experiments were performed on a 600 MHz Bruker spectrometer equipped with a prodigy cryoprobe. The NMR samples contained 50 μM ^{15}N,^{13}C-labeled Aβ42 buffered at pH 7.4 with 25 mM phosphate buffer, treated with 0 and 500 μM Ca-free Ator. The temperature was set at 278 K. A standard gradient-enhanced phase-sensitive Bruker pulse sequence was used for HSQC measurements, in which water signal was suppressed through a 3-9-19 WATERGATE element, and the scalar coupling between ^{15}N and ^{13}C nuclei was refocused in the indirect dimension. The acquired 2D free induction decays contained 256 and 1024 complex points in the ^{15}N and ^{1}H dimensions, respectively. The NMR spectra were processed using NMRPipe (75) and analyzed *via* Sparky (T.D. Goddard and D.G. Kneller; http://www.cgl.ucsf.edu/home/sparky). The peak assignments were obtained from the literature (76).

STD-NMR

The 1D ^{1}H STD-NMR experiments were conducted on a 900 MHz Bruker spectrometer equipped with a cryogenic probe. The NMR sample contained 300 μM Ca-free Ator and 5.0 μM Aβ42, that is, ligand:peptide molar ratio of 60:1, in 25 mM phosphate buffer at pH 7.4. The temperature was set at 310 K. A saturation block of 4 s, during which a train of 50 ms-long Gaussian pulses was applied at a field strength of 30 Hz at the specified frequencies, was used. Notably, the most upfield signal of Ator at ∼1.5 ppm was between 520 and 2000 Hz away from irradiation frequencies, well beyond the saturation bandwidth of the used Gaussian pulses. The irradiation at 60 ppm served as the reference spectrum, and the difference between saturated and reference spectra was shown as the STD spectra. The saturation frequencies were selected from the region of methyl proton resonances of Aβ42 and the region upfield to them (toward negative chemical shifts), far from the proton resonances of Ator. The total recycle delay was ca. 6 s. Suppression of residual water signal was achieved through a W5 WATERGATE element.

In silico experiments

The initial structure of Aβ40 was obtained from PDB (ID: 2LFM). This structure had been obtained in the 20 mM potassium phosphate buffer with 50 mM NaCl at pH 7.3 at 288 K and accordingly contains a central 3_{10}-helix from H13 to D23 and the N termini and C termini collapse against the helix (77). To work in parallel with experimental methods, two amino acids (Ile and Ala) were added to the C-terminal region of Aβ40 peptide using the Macromolecules module in Discovery Studio Visualizer (78). Afterward, Aβ42 was geometrically optimized at the B3LYP/6-31 ++G(d, p) level using the Gaussian 03 program (79). 3D structure of Ator molecule was extracted from the PDB (ID: 1HWK). To match with the structure used in the experimental section, the stereoisomer of hydroxyl groups was changed from R, R to R, S using the interactive version of the CORINA online server (80). Also, the hydrogen atom was removed from the carboxyl group. Finally, Gaussian 03 program was applied to geometrically optimize the structure of modified Ator with B3LYP/6-31 ++G(d, p) level.

Force field parameters and the topology for the Ator molecule were created by the antechamber module from the Amber Tools 14 suite (81) with AM1–bond charge correction charges. All MD simulations were performed using the GROMACS 2019.4 (82) with the AMBER99SB-ILDN force field (83) for Aβ peptide. First, an Aβ42 peptide was put in the center of a cubic box with 6.59 6.59 6.59 nm^{3} dimension so that the minimum distance between the peptide and the box walls was set to 1.2 nm. The periodic boundary conditions were considered. In this study, three MD simulations were done. In each simulation, a certain number of Ator molecules (2, 5, or 10) were inserted in the simulation box (Table S1). The Ator molecules were located and oriented randomly around the Aβ42 peptide. The obtained simulation systems were energy minimized with the steepest descent algorithm (84) in the vacuum phase to remove bad contacts. Then, water molecules were randomly added to the simulation boxes. The TIP3P model (85) was used to describe water molecules. To have the electroneutrality of the systems, appropriated Na^{+} counter ions were added to each system. Final prepared systems were energy minimized using the steepest descent and conjugate gradient methods (86).

After energy minimization, two equilibration steps for 1 ns each were performed: the first in the isochoric–isothermal (NVT) ensemble and the second in the isothermal–isobaric (NPT) ensemble. The constant temperature (300 K) and pressure (1 bar) were considered using V-rescale thermostat (87) and Berendsen barostat (88) with coupling constants of 0.1 and 1.0 ps, respectively. During the equilibration steps, the harmonic restraints with the force constants of 1000 kJ mol^{-1} nm^{-2} were applied on the coordinates of heavy atoms of Aβ42 peptide and Ator molecules. Finally, unrestrained MD simulation, production run, was performed for 500 ns under an

NPT ensemble with the same simulation conditions as for the second equilibration step. A time step of 2 fs was used to integrate the equations of motion using the leapfrog algorithm (89). The long-range electrostatic interactions were treated with the particle mesh Ewald (90) method, and a cutoff radius of 10 Å was employed for van der Waals interactions. All bond lengths involving hydrogen atoms were constrained with the LINCS algorithm (91). Maxwell distribution was applied to assign the initial velocities. The atomic coordinates were saved every 100 ps for all simulations. Molecular graphics were made with the VMD (92) and PyMol (93) programs.

Data availability

All 1D and 2D NMR data of Aβ42 aggregation will be shared upon request.

Supporting information—This article contains supporting information.

Acknowledgments—This work was supported by the Max Planck Society. We sincerely thank Gudrun Heim for the transmission electron microscopy measurements.

Author contributions—N. R.-G., K. G., and S. B. methodology; H. N. and L. K. formal analysis; H. N. and L. K. investigation; N. R.-G. and A. A. M.-M. data curation; H. N. writing–original draft; N. R.-G., S. B., C. G., and A. A. S. writing–review & editing; C. G. and A. A. S. supervision.

Funding and additional information—Financial support from the University of Tehran to H. N. is acknowledged. N. R.-G. acknowledges the Deutsche Forschungsgemeinschaft (German Research Foundation) for research grants RE 3655/2-1 and RE 3655/2-3.

Conflict of interest—The authors declare that they have no conflicts of interest with the contents of this article.

Abbreviations—The abbreviations used are: Aβ, amyloid-beta; AD, Alzheimer's disease; ADAS-Cog, Alzheimer's Disease Assessment Scale—Cognitive Subscale; APP, amyloid precursor protein; Ator, atorvastatin; Ator-Ca, atorvastatin-calcium; Ca-free Ator, calcium-free atorvastatin; DSSP, defined secondary structure protein; EGCG, epigallocatechin-3-gallate; h-bond, hydrogen bond; HSQC, heteronuclear single quantum coherence; MCA, monomer consumption assay; MD, molecular dynamics; NPI, Neuropsychiatric Inventory; PDB, Protein Data Bank; PR, Patton–Reeder; Rg, radius of gyration; RMSF, root mean square fluctuation; STD, saturation-transfer difference; TEM, transmission electron microscopy; ThT, thioflavin-T.

References

1. Patterson, K. R., Remmers, C., Fu, Y., Brooker, S., Kanaan, N. M., Vana, L., Ward, S., Reyes, J. F., Philibert, K., Glucksman, M. J., and Binder, L. I. (2011) Alzheimer disease characterization of prefibrillar tau oligomers *in vitro* and in Alzheimer disease. *J. Biol. Chem.* **286**, 23063–23076
2. Kametani, F., and Hasegawa, M. (2018) Reconsideration of amyloid hypothesis and tau hypothesis in Alzheimer's disease. *Front. Neurosci.* **12**, 1–11
3. Chong, F. P., Ng, K. Y., Koh, R. Y., and Chye, S. M. (2018) Tau proteins and tauopathies in Alzheimer's disease. *Cell. Mol. Neurobiol.* **38**, 965–980
4. Pauwels, K., Williams, T. L., Morris, K. L., Jonckheere, W., Vandersteen, A., Kelly, G., Schymkowitz, J., Rousseau, F., Pastore, A., Serpell, L. C., and Broersen, K. (2012) Structural basis for increased toxicity of pathological Aβ42:Aβ40 ratios in Alzheimer disease. *J. Biol. Chem.* **287**, 5650–5660
5. Rajasekhar, K., Chakrabarti, M., and Govindaraju, T. (2015) Function and toxicity of amyloid beta and recent therapeutic interventions targeting amyloid beta in Alzheimer's disease. *Chem. Commun.* **51**, 13434–13450
6. Busche, M. A., and Hyman, B. T. (2020) Synergy between amyloid-β and tau in Alzheimer's disease. *Nat. Neurosci.* **23**, 1183–1193
7. Lue, L.-F., Guerra, A., and Walker, D. G. (2017) Amyloid beta and tau as Alzheimer's disease blood biomarkers: Promise from new technologies. *Neurol. Ther.* **6**, 25–36
8. Huber, C. M., Yee, C., May, T., Dhanala, A., and Mitchell, C. S. (2018) Cognitive decline in preclinical Alzheimer's disease: Amyloid-beta versus tauopathy. *J. Alzheimers Dis.* **61**, 265–281
9. Du, X., Wang, X., and Geng, M. (2018) Alzheimer's disease hypothesis and related therapies. *Transl. Neurodegener.* **7**, 1–7
10. Chuang, E., Hori, A. M., Hesketh, C. D., and Shorter, J. (2018) Amyloid assembly and disassembly. *J. Cell Sci.* **131**, 1–18
11. Kelly, J. W. (2021) Does protein aggregation drive postmitotic tissue degeneration? *Sci. Transl. Med.* **13**, eaax0914
12. Sengupta, U., Nilson, A. N., and Kayed, R. (2016) The role of amyloid-β oligomers in toxicity, propagation, and immunotherapy. *EBioMedicine* **6**, 2352–3964
13. Cline, E. N., Bicca, M. A., Viola, K. L., and Klein, W. L. (2018) The amyloid-β oligomer hypothesis: Beginning of the third decade. *J. Alzheimers Dis.* **64**, 567–610
14. Citron, M. (2010) Alzheimer's disease: Strategies for disease modification. *Nat. Rev. Drug Discov.* **9**, 387–398
15. Xin, S.-H., Tan, L., Cao, X., Yu, J.-T., and Tan, L. (2018) Clearance of amyloid beta and tau in Alzheimer's disease: From mechanisms to therapy. *Neurotox. Res.* **34**, 733–748
16. Rygiel, K. (2016) Novel strategies for Alzheimer's disease treatment: An overview of anti-amyloid beta monoclonal antibodies. *Indian J. Pharmacol.* **48**, 629–636
17. Geylis, V., Kourilov, V., Meiner, Z., Nennesmo, I., Bogdanovic, N., and Steinitz, M. (2008) Human monoclonal antibodies against amyloid-beta from healthy adults. *Neurobiol. Aging* **26**, 597–606
18. Baghallab, I., Reyes-Ruiz, J. M., Abulnaja, K., Huwait, E., and Glabe, C. (2018) Epitomic characterization of the specificity of the anti-amyloid Aβ monoclonal antibodies 6E10 and 4G8. *J. Alzheimers Dis.* **66**, 1235–1244
19. Tolar, M., Abushakra, S., Hey, J. A., Porsteinsson, A., and Sabbagh, M. (2020) Aducanumab, gantenerumab, BAN2401, and ALZ-801—the first wave of amyloid-targeting drugs for Alzheimer's disease with potential for near term approval. *Alzheimers Res. Ther.* **12**, 1–10
20. Bu, X.-L., Rao, P. P., and Wang, Y.-J. (2016) Anti-amyloid aggregation activity of natural compounds: Implications for Alzheimer's drug discovery. *Mol. Neurobiol.* **53**, 3565–3575
21. Hernandez, A. M., Urbanke, H., Gillman, A. L., Lee, J., Ryazanov, S., Agbemenyah, H. Y., Benito, E., Jain, G., Kaurani, L., Grigorian, G., Leonov, A., Rezaei-Ghaleh, N., Wilken, P., Teran Arce, f. T., Wagner, J., *et al.* (2018) The diphenylpyrazole compound anle138b blocks Aβ channels and rescues disease phenotypes in a mouse model for amyloid pathology. *EMBO Mol. Med.* **10**, 32–47
22. Tanaka, F., Shibata, K., Monobe, Y., Akagi, K.-I., and Masuda, Y. (2020) Design and synthesis of β-strand-fixed peptides inhibiting aggregation of amyloid β-protein. *Bioorg. Med. Chem.* **28**, 1–10
23. Armiento, V., Spanopoulou, A., and Kapurniotu, A. (2020) Peptide-based molecular strategies to interfere with protein misfolding, aggregation, and cell degeneration. *Angew. Chem. Int. Ed. Engl.* **59**, 3372–3384
24. Jokar, S., Erfani, M., Bavi, O., Khazaei, S., Sharifzadeh, M., Hajiramezanali, M., Beiki, D., and Shamloo, A. (2020) Design of peptide-based inhibitor agent against amyloid-β aggregation: Molecular docking, synthesis and *in vitro* evaluation. *Bioorg. Chem.* **102**, 1–11
25. Stellato, F., Fusco, Z., Chiaraluce, R., Consalvi, V., Dinarelli, S., Placidi, E., Petrosino, M., Rossi, G. C., Minicozzi, V., and Morante, S. (2017) The

effect of β-sheet breaker peptides on metal associated amyloid-β peptide aggregation process. *Biophys. Chem.* **229**, 110–114
26. Nie, Q., Du, X.-G., and Geng, M.-Y. (2011) Small molecule inhibitors of amyloid β peptide aggregation as a potential therapeutic strategy for Alzheimer's disease. *Acta Pharmacol. Sin.* **32**, 545–551
27. Young, L. M., Ashcroft, A. E., and Radford, S. E. (2017) Small molecule probes of protein aggregation. *Curr. Opin. Chem. Biol.* **39**, 90–99
28. Giorgetti, S., Greco, C., Tortora, P., and Aprile, F. A. (2018) Targeting amyloid aggregation: An overview of strategies and mechanisms. *Int. J. Mol. Sci.* **19**, 1–27
29. Roche, J., Shen, Y., Lee, J. H., Ying, J., and Bax, A. (2016) Monomeric Aβ1–40 and Aβ1–42 peptides in solution adopt very similar Ramachandran map distributions that closely resemble random coil. *Biochemistry* **55**, 762–775
30. Sahoo, B. R., Cox, S. J., and Ramamoorthy, A. (2020) High-resolution probing of early events in amyloid-β aggregation related to Alzheimer's disease. *Chem. Commun.* **56**, 4627–4639
31. Masuda, Y., Uemura, S., Ohashi, R., Nakanishi, A., Takegoshi, K., Shimizu, T., Shirasawa, T., and Irie, K. (2009) Identification of physiological and toxic conformations in Aβ42 aggregates. *ChemBioChem* **10**, 287–295
32. Sarkar, B., Mithu, V. S., Chandra, B., Mandal, A., Chandrakesan, M., Bhowmik, D., Madhu, P. K., and Maiti, S. (2014) Significant structural differences between transient amyloid-β oligomers and less-toxic fibrils in regions known to harbor familial Alzheimer's mutations. *Angew. Chem. Int. Ed. Engl.* **126**, 7008–7012
33. Qiang, W., Yau, W.-M., Lu, J.-X., Collinge, J., and Tycko, R. (2017) Structural variation in amyloid-β fibrils from Alzheimer's disease clinical subtypes. *Nature* **541**, 217–221
34. Lee, J.-H., Ahn, N.-H., Choi, S.-B., Kwon, Y., and Yang, S.-H. (2021) Natural products targeting amyloid beta in Alzheimer's disease. *Int. J. Mol. Sci.* **22**, 1–17
35. Ji, H.-F., and Zhang, H.-Y. (2008) Multipotent natural agents to combat Alzheimer's disease. Functional spectrum and structural features. *Acta Pharmacol. Sin.* **29**, 143–151
36. Yanagisawa, D., Ibrahim, N. F., Taguchi, H., Morikawa, S., Hirao, K., Shirai, N., Sogabe, T., and Tooyama, I. (2015) Curcumin derivative with the substitution at C-4 position, but not curcumin, is effective against amyloid pathology in APP/PS1 mice. *Neurobiol. Aging* **36**, 201–210
37. Hung, V. W. S., Cheng, X. R., Li, N., Veloso, K., and Kerman, A. J. (2013) Electrochemical detection of amyloid-beta aggregation in the presence of resveratrol. *J. Electrochem. Soc.* **160**, 3097–3101
38. Al-Edresi, S., Alsalahat, I., Freeman, S., Aojula, H., and Penny, J. (2020) Resveratrol-mediated cleavage of amyloid beta (1–42) peptide: Potential relevance to Alzheimer's disease. *Neurobiol. Aging* **94**, 24–33
39. Ehrnhoefer, D., Bieschke, J., Boeddrich, A., Herbst, M., Masino, L., Lurz, R., Engemann, S., Pastore, A., and Wanker, E. E. (2008) EGCG redirects amyloidogenic polypeptides into unstructured, off-pathway oligomers. *Nat. Struct. Biol.* **15**, 558–566
40. Bieschke, J., Herbst, M., Wiglenda, T., Friedrich, R. P., Boeddrich, A., Schiele, F., Kleckers, D., Miguel Lopez del Amo, J., Grüning, B. A., Wang, Q., Schmidt, M. R., Lurz, R., Anwyl, R., Schnoegl, S., Fändrich, M., *et al.* (2012) Small-molecule conversion of toxic oligomers to nontoxic β-sheet–rich amyloid fibrils. *Nat. Chem. Biol.* **8**, 93–101
41. Du, W.-J., Guo, J.-J., Gao, M.-T., Hu, S.-Q., Dong, X.-Y., Han, Y.-F., Liu, F.-F., Jiang, S., and Sun, Y. (2015) Brazilin inhibits amyloid β-protein fibrillogenesis, remodels amyloid fibrils and reduces amyloid cytotoxicity. *Sci. Rep.* **5**, 1–10
42. Wang, Q., Yu, X., Patal, K., Hu, R., Chuang, S., Zhang, G., and Zheng, J. (2015) Tanshinones inhibit amyloid aggregation by amyloid-β peptide, disaggregate amyloid fibrils, and protect cultured cells. *ACS Chem. Neurosci.* **4**, 1004–1015
43. Niu, Z., Sarkar, R., Aichler, M., Wester, H.-J., Yousefi, B. H., and Reif, B. (2020) Mapping the binding interface of PET tracer molecules and Alzheimer disease Aβ fibrils by using MAS solid-state NMR spectroscopy. *ChemBioChem* **21**, 2495–2502
44. Stancu, C., and Sima, A. (2007) Statins: Mechanism of action and effects. *J. Cell. Mol. Med.* **5**, 378–387
45. Sirtori, C. R. (2014) The pharmacology of statins. *Pharmacol. Res.* **88**, 3–11
46. Weitz-Schmidt, G. (2002) Statins as anti-inflammatory agents. *Trends Pharmacol. Sci.* **23**, 482–486
47. Petanceska, S. S., DeRosa, S., Olm, V., Diaz, N., Sharma, A., Thomas-Bryant, T., Duff, K., Pappolla, M., and Refolo, L. M. (2002) Statin therapy for Alzheimer's disease. *J. Mol. Neurosci.* **19**, 155–161
48. Cibickova, L., Radomir, H., Stanislav, M., Norbert, C., Helena, Z., Daniel, J., Alena, T., Eva, B., and Vladimir, P. (2009) The influence of simvastatin, atorvastatin and high-cholesterol diet on acetylcholinesterase activity, amyloid beta and cholesterol synthesis in rat brain. *Steroids* **74**, 13–19
49. Kurata, T., Miyazaki, K., Kozuki, M., Panin, V. L., Morimoto, N., Ohta, Y., Nagai, M., Ikeda, Y., Matsuura, T., and Abe, K. (2011) Atorvastatin and pitavastatin improve cognitive function and reduce senile plaque and phosphorylated tau in aged APP mice. *Brain Res.* **1371**, 161–170
50. Zhao, L., Chen, T., Wang, C., Li, G., Zhi, W., Yin, J., Wan, Q., and Chen, L. (2016) Atorvastatin in improvement of cognitive impairments caused by amyloid β in mice: Involvement of inflammatory reaction. *BMC Neurol.* **16**, 18
51. Corrao, G., Ibrahim, B., Nicotra, F., Zambon, A., Merlino, L., Pasini, T. S., Catapano, A. L., and Mancia, G. (2013) Long-term use of statins reduces the risk of hospitalization for dementia. *Atherosclerosis* **230**, 171–176
52. Martins, W. C., dos Santos, V. V., dos Santos, A. A., Vandresen-Filho, S., Dal-Cim, T. A., de Oliveira, K. A., Mendes-de-Aguiar, C. B., Farina, M., Prediger, R. D., Viola, G. G., and Tasca, C. I. (2015) Atorvsastatin prevents cognitive deficits induced by intracerebroventricular amyloid-beta1-40 administration in mice: Involvement of glutamatergic and antioxidant sytems. *Neurotox. Res.* **28**, 32–42
53. Kurata, T., Miyazaki, K., Morimoto, N., Kawai, H., Ohta, Y., Ikeda, Y., and Abe, K. (2013) Atorvastatin and pitavastatin reduce oxidative stress and improve IR/LDL-R signals in Alzheimer's disease. *Neurol. Res.* **35**, 193–205
54. Xuan, K., Zhao, T., Qu, G., Liu, H., Chen, X., and Sun, Y. (2020) The efficacy of statins in the treatment of Alzheimer's disease: A meta-analysis of randomized controlled trial. *Neurol. Sci.* **41**, 1391–1404
55. Kueper, J. K., Speechley, M., and Montero-Odasso, M. (2018) The Alzheimer's disease assessment scale–cognitive subscale (ADAS-Cog): Modifications and responsiveness in pre-dementia populations. A narrative review. *J. Alzheimers Dis.* **63**, 423–444
56. Cummings, J. L., Mega, M., Gray, K., Rosenberg-Thompson, S., Carusi, D. A., and Gornbein, J. (1994) The neuropsychiatric inventory: Comprehensive assessment of psychopathology in dementia. *Neurology* **44**, 2308–2314
57. Itkin, A., Dupres, V., Dufrêne, Y. F., Bechinger, B., Ruysschaert, J.-M., and Raussens, V. (2011) Calcium ions promote formation of amyloid β-peptide (1–40) oligomers causally implicated in neuronal toxicity of Alzheimer's disease. *PLoS One* **6**, 1–10
58. Rao, P. P., Mohamed, T., Teckwani, K., and Tin, G. (2015) Curcumin binding to beta amyloid: A computational study. *Chem. Biol. Drug Des.* **86**, 813–820.
59. Li, G., and Pomès, R. (2013) Binding mechanism of inositol stereoisomers to monomers and aggregates of Aβ (16-22). *J. Phys. Chem. B* **117**, 6603–6613.
60. Liu, F. F., Dong, X. Y., He, L., Middelberg, A. P., and Sun, Y. (2011) Molecular insight into conformational transition of amyloid β-peptide 42 inhibited by (−)-epigallocatechin-3-gallate probed by molecular simulations. *J. Phys. Chem. B* **115**, 11879–11887.
61. Liu, F. F., Ji, L., Dong, X. Y., and Sun, Y. (2009) Molecular insight into the inhibition effect of trehalose on the nucleation and elongation of amyloid β-peptide oligomers. *J. Phys. Chem. B* **113**, 11320–11329.
62. Santini, S., Mousseau, N., and Derreumaux, P. (2004) In silico assembly of Alzheimer's Aβ16-22 peptide into β-sheets. *J. Am. Chem. Soc.* **126**, 11509–11516
63. Viegas, A., Manso, J., Nobrega, F. L., and Cabrita, E. J. (2011) Saturation-transfer difference (STD) NMR: A simple and fast method for ligand screening and characterization of protein binding. *J. Chem. Educ.* **88**, 990–994

64. Hooft, R. W., Sander, C., Scharf, M., and Vriend, G. (1996) The PDBFINDER database: A summary of PDB, DSSP and HSSP information with added value. *Comput. Appl. Biosci.* **12**, 525–529.
65. Nath, S., Goodwin, J., Engelborghs, Y., and Pountney, D. L. (2011) Raised calcium promotes α-synuclein aggregate formation. *Mol. Cell. Neurosci.* **46**, 516–526
66. Fassbender, K., Stroick, M., Bertsch, T., Ragoschke, A., Kuehl, S., Walter, S., Walter, J., Brechtel, K., Muehlhauser, F., von Bergmann, K., and Lütjohann, T. (2002) Effects of statins on human cerebral cholesterol metabolism and secretion of Alzheimer amyloid peptide. *Neurology* **59**, 1257–1258
67. Jiang, L., Liu, C., Leibly, D., Landau, M., Zhao, M., Hughes, M. P., and Eisenberg, D. S. (2013) Structure-based discovery of fiber-binding compounds that reduce the cytotoxicity of amyloid beta. *Elife* **2**, e00857
68. Masuda, Y., Fukuchi, M., Yatagawa, T., Tada, M., Takeda, K., Irie, K., Akagi, K.-I., Monobe, Y., Imazawa, T., and Takegoshi, K. (2011) Solid-state NMR analysis of interaction sites of curcumin and 42-residue amyloid β-protein fibrils. *Bioorg. Med. Chem.* **19**, 5967–5974
69. Galanakis, P. A., Bazoti, F. N., Bergquist, J., Markides, K., Spyroulias, G. A., and Tsarbopoulos, A. (2011) Study of the interaction between the amyloid beta peptide (1-40) and antioxidant compounds by nuclear magnetic resonance spectroscopy. *Biopolymers* **96**, 316–327
70. Ladiwala, A. A., Lin, J. C., Bale, S. S., Marcelino-Cruz, A. M., Bhattacharya, M., Dordick, J. S., and Tessier, P. M. (2010) Resveratrol selectively remodels soluble oligomers and fibrils of amyloid Abeta into off-pathway conformers. *J. Biol. Chem.* **285**, 24228–24237
71. Sato, M., Murakami, K., Uno, M., Nakagawa, Y., Katayama, S., Akagi, K.-i., Masuda, Y., Takegoshi, K., and Irie, K. (2013) Site-specific inhibitory mechanism for amyloid beta42 aggregation by catechol-type flavonoids targeting the Lys residues. *J. Biol. Chem.* **288**, 23212–23224
72. Ryan, T. M., Caine, J., Mertens, H. D., Kirby, N., Nigro, J., Breheney, K., Waddington, L. J., Streltsov, V. A., Curtain, C., Masters, C. L., and Roberts, B. R. (2013) Ammonium hydroxide treatment of Aβ produces an aggregate free solution suitable for biophysical and cell culture characterization. *PeerJ* **1**, e73
73. Kumar, S., Rezaei-Ghaleh, N., Terwel, D., Thal, D. R., Richard, M., Hoch, M., Mc Donald, J. M., Wüllner, U., Glebov, K., Heneka, M. T., Walsh, D. M., Zweckstetter, M., and Walter, J. (2011) Extracellular phosphorylation of the amyloid β-peptide promotes formation of toxic aggregates during the pathogenesis of Alzheimer's disease. *EMBO J.* **30**, 2255–2265
74. Xue, C., Lin, T. Y., Chang, D., and Guo, Z. (2017) Thioflavin T as an amyloid dye: Fibril quantification, optimal concentration and effect on aggregation. *R. Soc. Open Sci.* **4**, 1–12
75. Delaglio, F., Grzesiek, S., Vuister, G. W., Zhu, G., Pfeifer, J., and Bax, A. (1995) NMRPipe: A multidimensional spectral processing system based on UNIX pipes. *J. Biomol. NMR* **6**, 277–293
76. Rezaei-Ghaleh, N., Giller, K., Becker, S., and Zweckstetter, M. (2011) Effect of zinc binding on β-amyloid structure and dynamics: Implications for Aβ aggregation. *Biophys. J.* **101**, 1202–1211
77. Vivekanandan, S., Brender, j. R., Lee, S. Y., and Ramamoorthy, A. (2011) A partially folded structure of amyloid-beta(1–40) in an aqueous environment. *Biochem. Biophys. Res. Commun.* **411**, 312–316
78. Biovia, D. S. (2017) *Discovery Studio Visualizer*. San Diego, CA: 936
79. Frisch, M. J., Trucks, G. W., Schlegel, H. B., Scuseria, G. E., Robb, M. A., Cheeseman, J. R., and Pople, J. A. (2004) *Gaussian 03, Revision C. 02*, Gaussian Inc, Wallingford, CT
80. Sadowski, J., Gasteiger, J., and Klebe, G. (1994) Comparison of automatic three-dimensional model builders using 639 X-ray structures. *J. Chem. Inform. Comput. Sci.* **34**, 1000–1008
81. Macke, T. J., Svrcek-Seiler, W. A., Brown, R. A., Kolossváry, I., Bomble, Y. J., Case, D. A., and Wang, J. (2010) *AmberTools Users' Manual*,
82. Lindahl, E., Abraham, M. J., Hess, B., and Spoel, D. V. D. (2020) GROMACS 2019.6 manual (2019.6). *Zenodo*. https://doi.org/10.5281/zenodo.3685925
83. Lindorff-Larsen, K., Piana, S., Palmo, K., Maragakis, P., Klepeis, J. L., Dror, R. O., and Shaw, D. E. (2010) Improved side-chain torsion potentials for the Amber ff99SB protein force field. *Proteins* **78**, 1950–1958.
84. Curry, H. B. (1944) The method of steepest descent for non-linear minimization problems. *Q. Appl. Math.* **2**, 258–261.
85. Jorgensen, W. L., Chandrasekhar, J., Madura, J. D., Impey, R. W., and Klein, M. L. (1983) Comparison of simple potential functions for simulating liquid water. *J. Chem. Phys.* **79**, 926–935.
86. Polyak, B. T. (1969) The conjugate gradient method in extremal problems. *USSR Comput. Math. Math. Phys.* **9**, 94–112.
87. Bussi, G., Donadio, D., and Parrinello, M. (2007) Canonical sampling through velocity rescaling. *J. Chem. Phys.* **126**, 014101.
88. Berendsen, H. J., Postma, J. V., van Gunsteren, W. F., DiNola, A. R. H. J., and Haak, J. R. (1984) Molecular dynamics with coupling to an external bath. *J. Chem. Phys.* **81**, 3684–3690.
89. Van Gunsteren, W. F., and Berendsen, H. J. (1988) A leap-frog algorithm for stochastic dynamics. *Mol. Simul.* **1**, 173–185.
90. Sagui, C., and Darden, T. A. (1999) Molecular dynamics simulations of biomolecules: Long-range electrostatic effects. *Annu. Rev. Biophys. Biomol. Struct.* **28**, 155–179.
91. Hess, B., Bekker, H., Berendsen, H. J., and Fraaije, J. G. (1997) LINCS: A linear constraint solver for molecular simulations. *J. Comput. Chem.* **18**, 1463–1472.
92. Humphrey, W., Dalke, A., and Schulten, K. (1996) VMD: Visual molecular dynamics. *J. Mol. Graph.* **14**, 33–38.
93. DeLano, W. L. (2002) Pymol: An open-source molecular graphics tool. *CCP4 Newsl. Protein Crystallogr.* **40**, 82–92.